



Regularized Phase-Based Conductivity Mapping Using MRI

THESIS

submitted in partial fulfillment of the
requirements for the degree of

MASTER OF SCIENCE

in

PHYSICS

Author : Konstantin Iakovlev
Student ID : s2109190
Supervisor : Dr. ir. W. Brink, Dr. L. Bossoni
2nd corrector : Prof.dr.ir. T.H. Oosterkamp

Leiden, The Netherlands, November 1, 2019

Regularized Phase-Based Conductivity Mapping Using MRI

Konstantin Iakovlev

Huygens-Kamerlingh Onnes Laboratory, Leiden University
P.O. Box 9500, 2300 RA Leiden, The Netherlands

November 1, 2019

Abstract

Phase-based conductivity mapping using MRI data contains an assumption of locally constant complex permittivity and use of a differential operator which result in significant inaccuracies at tissue boundaries and amplification of noise in data. This work focuses on the implementation of an iterative model-based nonlinear optimization algorithm that aims to surpass these rising inaccuracies. The algorithm is designed to optimize conductivity maps using phase data acquired from MRI. In addition to optimization, the algorithm focuses on regularization which further improves the optimized outcome of the conductivity maps.

Successful results are demonstrated using both simulated as well as phantom data. The comparison between results of a conventional phase-based conductivity mapping and the iterative algorithm shows improved accuracy for the latter. In addition, the model-based algorithm possesses potential for reduced acquisition time as it is capable of reconstructing accurate conductivity maps with relatively low SNR. In the future, experiments on in-vivo data can be performed. Additionally, to improve the accuracy of the conductivity maps even further, implementation of optimal methods to determine regularization parameters and regularization functions is possible.

Acknowledgement

I would like to take an opportunity to acknowledge and thank several people and colleagues that made this research and thesis possible.

First of all, I would like to thank Dr. Wyger M. Brink and Dr. Itamar

Ronen for welcoming and presenting me with variety of realizable projects and the opportunity to work on this project in particular at Leiden University Medical Center. You have been patient and guiding throughout the learning process of this project.

Secondly, I would like to express my deepest gratitude to ir. Reijer L. Leijsen and Dr. Wyger M. Brink for their cooperation, expertise on the subject, patience and support. Mastering programming and a number of implementations on Python would have been hard-pressed within a limited amount of time without your help. A special 'thank you' for trusting me throughout this research.

Additionally, I would like to commend Dr. Lucia Bossoni, Dr. Wyger M. Brink, ir. Reijer L. Leijsen, and Loes Huijnen for being a part of weekly EPT meetings. Thank you for your expertise and willingness to participate in scientific discussions.

Contents

1	Introduction	7
2	Mathematical & Physical concepts	9
2.1	Mathematical concepts	9
2.1.1	Convolution	9
2.1.2	Fourier transform	11
2.1.3	Convolution theorem	12
2.1.4	Finite difference	13
2.2	Physical concepts	14
2.2.1	Principles of MRI and SE scan	14
3	Theory & Methods	19
3.1	Phase-based conductivity mapping	19
3.2	Inverse Laplacian approach	22
3.2.1	Approach without regularization	26
3.2.2	Approach with regularization	29
4	Results & Discussion	33
4.1	Approach without regularization	33
4.2	Approach with regularization	39
4.2.1	Simulated data	39
4.2.2	Phantom data	44
5	Conclusion	47

Introduction

Magnetic Resonance Imaging or MRI is an imaging technique which probes the spin dynamics of atoms within the bodies using strong magnetic fields. These dynamics can then be detected and the information can be exploited to produce images of the soft tissue throughout the entire body. The main advantage of the technique is that it is practically harmless for the patients as the radiation used is non-ionizing. Initially named Nuclear Magnetic Resonance (NMR), the MRI was later introduced to its current name as it revoked unease in the patients [1].

MRI was developed by Paul Lauterbur together with Peter Mansfield in 1970s nearly 40 years after the nuclear resonance was first observed by Isidor Rabi [2]. Along with the imaging of the different types of tissue in the human body, it was quickly discovered that characterization of the dielectric tissue properties with the data from the MRI system was possible [3]. These dielectric properties, mainly, are the electrical characteristics of tissue called permittivity and conductivity which depend on water content, cell size and the mobility of ions in the tissue [4].

In 1991, first publications were made with relevant results on measuring the electrical properties exploiting radiofrequency magnetic fields in MRI [5]. However, it was not until 2009 that the concepts of reconstructing electrical properties from radiofrequency field data were advanced [6]. Such concepts to reconstruct conductivity maps are a part of electrical properties tomography (EPT) branch of studies which aims to establish effective and accurate ways to create conductivity maps of different types of tissue.

EPT using data from MRI has been demonstrated in phantoms, volunteers and limited patient studies [7,8]. Main applications of the conductivity maps are hyperthermia treatment planning, transcranial magnetic

stimulation and transcranial current stimulation, specific absorption rate calculations, and diagnostics [9,10,11,12]. The absorption rate calculation is particularly important as it is one of the key factors in high field MRI applications. In the diagnostic context, it has been shown that conductivity increases in tumor cells which adds the contrast for tumor detection [4,13].

The EPT, thus far, involves assumptions which violate inhomogeneities of the electrical properties within the tissue and the use of the differential operators in calculations which amplifies the impurities in the data. Therefore, the main disadvantages in the EPT have been rising boundary errors as well as noise amplification effects resulting in relatively low signal-to-noise ratio (SNR) [8]. There have been several proposed methods to solve these issues [8,14,15]. A few attempts concerning integral operators have been made to avoid the homogeneous assumptions. However, these methods suffer from an increased computational complexity while solving either permittivity or conductivity from combined Maxwell equations involving vortices of the complex data [16,17].

In this work, we focus on the regularized inverse approach as opposed to forward conductivity mapping approach. The novel method was first introduced by Kathleen Ropella, et al., in 2016 [9]. The aim of this method is to reduce the noise amplification factors and minimize the boundary errors. We use the method to program an algorithm designed to reconstruct three dimensional conductivity maps from numerical simulations and MRI scan data on phantoms.

In the future, additional experiments of the algorithm of the inverse approach can be made with in-vivo data.

Chapter 2

Mathematical & Physical concepts

In this chapter, we introduce several mathematical as well as physical concepts which we will discuss briefly yet thoroughly. We will limit the number of the concepts to only the ones that are relevant and helpful for our work. For the purpose of simplicity, we leave the proofs of the following concepts and their identities for the reader to find in the references for further reading.

2.1 Mathematical concepts

2.1.1 Convolution

In computer science and image processing within the medical world concerning mapping different properties in various subjects and patients, deep knowledge of mathematical analysis is required in which, more precisely, the functional analysis is focused on [18]. Medical images as well as diverse range of filters required to enhance or clear out these images can be represented as matrices or, more accurately, as functions. These filters and images must be combined together in order to produce a new image. In other words, two functions must be combined in a way so that they produce a third function. This is done by a mathematical operation known as *convolution* which is a vital element in the field of signal processing [19].

Convolution can be viewed as the following equation:

$$h(x) = f(x) * g(x) \quad (2.1)$$

where f is our input function i.e. our initial image, g is characterization of the kernel or filter applied to our image and h is the new produced image

function. Here, the asterisk, $*$, symbolises the convolution operation. In this operation, the input is decomposed into an infinite number of individual delta functions each of which produces a shifted and scaled version of the response to the kernel. The final output is then a summed combination of all the individual responses.

Due to the dual nature of signals in the field of signal processing, operations can be either continuous or discrete. In both of these cases, each individual value in the output image is affected by a section of the input image which is weighted by the kernel response flipped from one side to another. In the continuous case, the input and the responding filter are multiplied and integrated over infinite distance while in the discrete case, the two are multiplied and summed instead. This can be visualised by the following equations corresponding to the continuous and the discrete cases, respectively:

$$h(x) = f(x) * g(x) = \int_{-\infty}^{\infty} f(x-y)g(y)dy, \quad (2.2)$$

$$h[n] = f[n] * g[n] = \sum_{m=-\infty}^{\infty} f[n-m]g[m]. \quad (2.3)$$

In addition to the information above, we demonstrate algebraic properties of the convolution. We limit our selection to only the properties that are relevant for this work.

Commutativity:

$$f * g = g * f, \quad (2.4)$$

Associativity with and without a scalar multiplication, respectively:

$$a(f * g) = (af) * g = f * (ag), \quad (2.5)$$

$$(f * g) * h = f * (g * h), \quad (2.6)$$

Distributivity:

$$f * (g + h) = (f * g) + (f * h), \quad (2.7)$$

Relation with differentiation:

$$(f * g)' = f' * g = f * g', \quad (2.8)$$

Complex conjugation:

$$\overline{f * g} = \bar{f} * \bar{g}. \quad (2.9)$$

2.1.2 Fourier transform

In image processing, the Fourier Transform is an important tool. It is used to decompose an image, which can be described as a function of spatial coordinates, into a number of sine and cosine components. This, in the field of image processing, corresponds to moving the input image from its spatial domain into the spatial frequency domain which can also be called the Fourier domain. The Fourier domain consists of a set of points each of which represents a particular spatial frequency contained in the image.

The continuous Fourier Transform (CFT) of a function $f(t)$ which may be composed of both real and complex components, is defined as follows [20]:

$$F(x) = \mathcal{F}\{f(t)\} = \int_{-\infty}^{\infty} f(t)e^{-2\pi itx} dt. \quad (2.10)$$

To observe the reversibility of the transform, another transform with $e^{2\pi itx}$ is applied to already existing Fourier Transform which yields the original function. This is known as the inverse Fourier Transform [21]:

$$f(t) = \mathcal{F}^{-1}\{F(x)\} = \int_{-\infty}^{\infty} F(x)e^{2\pi itx} dx. \quad (2.11)$$

The exact definitions of the CFT may vary in literature, mainly by dropping 2π from the exponent and adding a coefficient in front of the integral to honour energy conservation principles. However, for simplicity of notation, we stick to the definitions above.

In the realm of digital images, the discrete Fourier Transform (DFT) is used as the images consist of a number of discrete pixels and not continuous signals. The DFT and the inverse DFT of an N -element-long sequence $\{x_n\} := x_0, x_1, \dots, x_{N-1}$ are defined, respectively, as:

$$X_k = \sum_{n=0}^{N-1} x_n e^{-2\pi i kn/N}, \quad (2.12)$$

$$x_n = \frac{1}{N} \sum_{k=0}^{N-1} X_k e^{2\pi i kn/N}. \quad (2.13)$$

Furthermore, as the images are hardly ever one dimensional, we define the DFT and inverse DFT for an N -dimensional case, respectively:

$$X_{a,\dots,b} = \sum_{n=0}^{N-1} \dots \sum_{m=0}^{M-1} x_{n,\dots,m} e^{-2\pi i (an/N + \dots + bm/M)}, \quad (2.14)$$

$$x_{n,\dots,m} = \frac{1}{N} \dots \frac{1}{M} \sum_{a=0}^{N-1} \dots \sum_{b=0}^{M-1} X_{a,\dots,b} e^{2\pi i(an/N + \dots + bm/M)}. \quad (2.15)$$

The DFT converts a sequence of equally spaced samples of a function into a new sequence of samples which are equally spaced resulting in a sequence of the same length. This means that the DFT includes all the frequencies forming the image and therefore it is a direct reason why the DFT produces a new image in the frequency domain without changing its size [22].

In the image reconstruction and analysis, the explicit calculation of the DFT can be computationally rather heavy even when the exponential factors are precomputed. Henceforth, in this work, we will use the computationally more efficient fast Fourier Transform (FFT) which is an algorithm that can compute DFT and inverse DFT. We will not specify any of the FFT algorithms in this work as the functions for the FFT are easily accessible in nearly every mainstream programming language and the sole purpose of understanding of the FFT, in this work, is its ability of moving a function into the Fourier domain faster than the calculation of the regular DFT. Nonetheless, a list of various FFT algorithms and their descriptions can be found in Ref. [23].

2.1.3 Convolution theorem

Now that both the Fourier Transform and the Convolution have been explained, we can move on to the *convolution theorem* which states that under appropriate circumstances, the Fourier Transform of the convolution of two signals or images equals an operation of pointwise product of both images in the Fourier domain. This can be elucidated with the following equation:

$$\mathcal{F}\{f * g\} = \mathcal{F}\{f\} \cdot \mathcal{F}\{g\}, \quad (2.16)$$

which showcases that a convolution in one domain is just a pointwise product in the Fourier domain. This can obviously be reversed in which case we get that a pointwise product is a convolution in another domain:

$$\mathcal{F}\{f \cdot g\} = \mathcal{F}\{f\} * \mathcal{F}\{g\}. \quad (2.17)$$

These two properties do not change under the operation of the inverse Fourier Transform as they only depend on the fact that the domain must change. The direction of the domain change is irrelevant and hence we can write out nearly identical properties with the inverse Fourier Transform:

$$\mathcal{F}^{-1}\{f * g\} = \mathcal{F}^{-1}\{f\} \cdot \mathcal{F}^{-1}\{g\}, \quad (2.18)$$

$$\mathcal{F}^{-1}\{f \cdot g\} = \mathcal{F}^{-1}\{f\} * \mathcal{F}^{-1}\{g\}. \quad (2.19)$$

The convolution theorem is useful for this work mostly from the computational point of view as the pointwise multiplication is obviously much faster to perform than a lengthy decomposition and assembly of individual delta functions that produce various versions of responses required for the complete convolution.

2.1.4 Finite difference

Boundary value problems are frequent in image processing which is why different finite difference methods are commonly used to approximate derivatives in order to obtain numerical solution of the differential equations. One such finite difference takes the mathematical expression of $f(x + b) - f(x + a)$. Since the method presents an approximation of a derivative, the term finite difference approximation is also often used. The relation of the methods with derivatives can be found in Ref. [24].

Depending on the applications used, three forms of finite differences are commonplace. Forward $\Delta_h[f](x)$, Backward $\nabla_h[f](x)$, and Central $\delta_h[f](x)$ differences on an arbitrary function are displayed in the equations (2.20) – (2.22), respectively [25].

Forward difference shows the difference value in the form of subtraction between a function value at a selected point and another function value at a new point with added spacing h :

$$\frac{\Delta_h[f](x)}{h} = \frac{f(x + h) - f(x)}{h}. \quad (2.20)$$

Backward difference shows a value of the difference between function values at a selected point and at a point $x - h$ instead of $x + h$:

$$\frac{\nabla_h[f](x)}{h} = \frac{f(x) - f(x - h)}{h}. \quad (2.21)$$

Finally, in Central difference, a point of interest is taken and two points are taken around it with equal spacing and then the function values at both of these points are subtracted:

$$\frac{\delta_h[f](x)}{h} = \frac{f(x + h) - f(x - h)}{h}. \quad (2.22)$$

The spacing h can be either a variable or a constant depending on the application. In this work, we operate mainly with discrete functions since, in the image processing, the function values are spatially restricted by resolution values and therefore h will be a constant as it is dependent on factors of resolution.

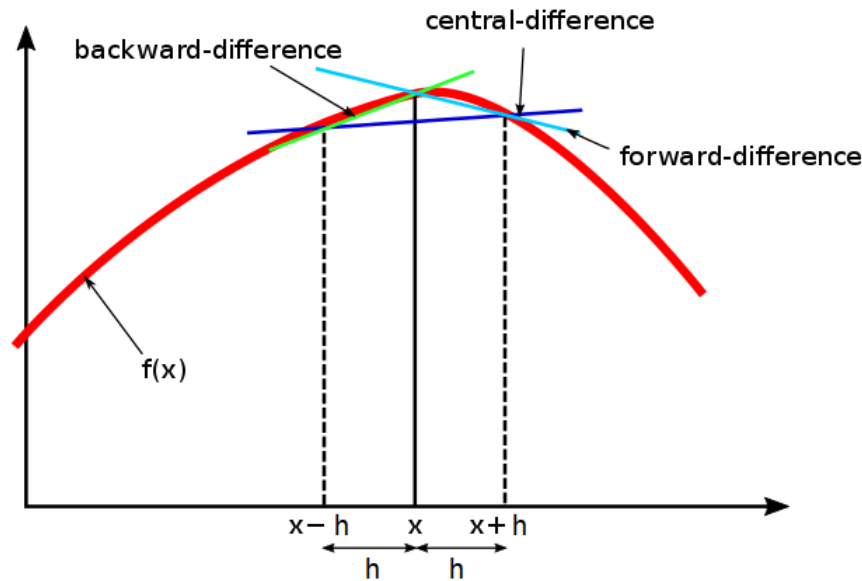


Figure 2.1: Backward, Central and Forward finite differences on a function at a selected point x and a random spacing value h . Out of the three approximations, the Central difference is the most accurate [26]. Plot obtained and modified from https://www.wikiwand.com/en/Finite_difference, 16/09/2019.

2.2 Physical concepts

2.2.1 Principles of MRI and SE scan

In order to explain the type of data we acquire, we need to have a general description of the techniques and physics behind the source of images. In this project, the data is obtained from a clinical imaging modality called magnetic resonance imaging (MRI).

MRI is non-invasive imaging technology which creates a spatial map of nuclei of hydrogen atoms (mostly in water and lipids). The images can be acquired in both two-dimensional as well as three-dimensional geometries. The intensity of the image depends on the density of protons in a bounded spatial area [27]. Using a strong magnetic field and radiofrequency current pulses directed to go through the object, the MRI alters the spin directions of the protons within the tissue of the object. The relaxation times, i.e. the time it takes the spins to point in their initial directions, can be obtained which will provide information about the physical properties of the tissue.

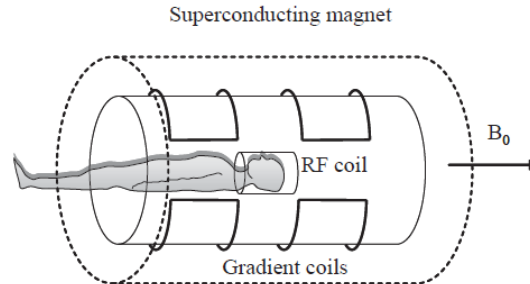


Figure 2.2: Three major parts of the MRI system. Superconducting magnet, RF transmitter and receiver, and, for simplicity, only one gradient coil.

The MRI system consists of three major parts: a superconducting magnet, radiofrequency transmitter and receiver, and three different magnetic field gradient coils. The simplified schematic image of the system can be found in Figure 2.2. Clinical field strengths of, B_0 , are 1.5 and 3 T which are 60 000 and 140 000 times stronger than the earth's magnetic field, respectively. Research systems at higher field strengths are coming up.

The protons, being charged particles in different types of tissue, can be thought of as small magnets as they carry spins which are an intrinsic form of describing an angular momentum, P , characterized by quantum numbers. Due to this spin, each particle also has a magnetic moment μ which gives them magnetic properties. The magnetic moment μ is directly proportional to the magnitude of the angular momentum of the proton:

$$|\vec{\mu}| = \gamma|\vec{P}|, \quad (2.23)$$

where γ is gyromagnetic ratio. While being outside the magnetic field, the magnitude of each magnetic moment is fixed. However, their orientation is completely random resulting in the net magnetization M being zero. When the protons are in the magnetic field, due to the nature of quantum mechanics, the magnetic moment can have only two quantized values. These values are the alignments at angles $\theta = \pm 54.7^\circ$ with respect to the direction of the B_0 field [27]. The positive value is termed as parallel and negative as anti-parallel which refer to the z -component of the magnetic moment μ and to the fact that μ is aligned with respect to the direction of B_0 .

When the magnetic moment of the protons is aligned with respect to B_0 at an angle of 54.7° , the B_0 field tries to align the magnetic moment with itself creating a torque, C , which is a cross product of both magnetic fields μ and B_0 :

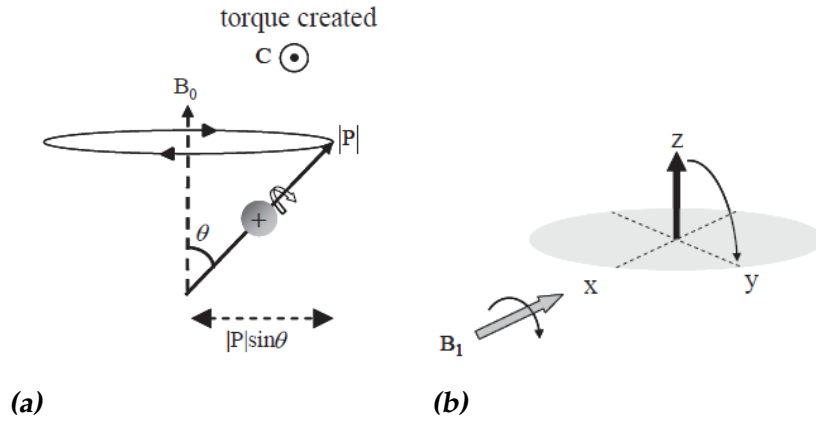


Figure 2.3: (a) Precessing movement of the spins around the B_0 field at an angle θ . (b) The flip of the spin direction to the xy -plane as RF pulse is applied to the system along x -axis.

$$\vec{C} = \vec{\mu} \times \vec{B}_0 = |\mu||B_0|\sin\theta\hat{k}, \quad (2.24)$$

where \hat{k} is unit vector perpendicular to both $\vec{\mu}$ and \vec{B}_0 . The torque then forces the protons into the precessing movement around B_0 . This is due to the tangential direction of the torque with respect to magnetic moment shown in Figure 2.3a. The frequency of the precess is directly proportional to the B_0 field:

$$\omega = \gamma|B_0|. \quad (2.25)$$

This frequency is called Larmor frequency, ω_0 . Its derivation is irrelevant for our work but can be found in Ref. [27].

While in the magnetic field, B_0 , all the protons are precessing in the parallel or anti-parallel directions creating a net magnetization along the z -axis parallel to the B_0 field. This net magnetization is calculated by the vector sum of individual components. The magnetization only has the z -component as the components along the x - and y -axes cancel each other.

The net magnetization can be rotated by applying short radiofrequency (RF) pulses perpendicular to the static field B_0 . The magnetic component of these pulses called B_1 field creates a torque that forces the net magnetization to rotate towards the xy -plane without affecting Larmor frequency. This process is demonstrated in Figure 2.3b. After these energy pulses are being turned on and off, an electrical signal can be detected due to Faraday's law of induction which states that the varying magnetic flux over

time induces an electrical voltage. However, these signals do not yet contain any spatial information. In order to gain spatial information, the three gradient coils are, in turns, switched on to generate magnetic field gradients along the three axes independently. The Larmour frequency describing the precess motion of the protons depends on the magnitude of B_0 field and consequently on its gradients in independent directions encoding the spins spatially [27].

Before the RF pulses are applied, the system is in the equilibrium magnetization state with a sole M_z -component. When the pulses are switched on, they create a non-equilibrium system where both M_x - and M_y -components are non-zero. After the pulses are switched off, the system decays back into the equilibrium which is characterized by two relaxation times: spin-lattice, T_1 , and spin-spin, T_2 , relaxations. T_1 governs only the z-component of magnetization and T_2 governs the x- and y-components. Relaxation times alter greatly depending on the consistency of the object which is why they can be used to classify the type of the tissue [27,28,29].

The sequence used to acquire data in this work is called Spin Echo (SE). In order to explain it, first consider only M_z -component of the net magnetization without B_1 field in the system. As the first step, an RF pulse is applied so that it flips the net magnetization to xy-plane without losing the value in comparison to the initial M_z . This pulse is termed 90 degree pulse. Due to inhomogeneities in strength of local magnetic field in the system, some spins speed up and some slow down, as the net moment precesses. This is what makes the signal decay. Another pulse, a 180 degree pulse, is applied to flip the spins around so that the slower ones are ahead of the main moment and faster ones are behind. At last, the fast moments catch up with the main moment, while the main moment catches up with the slow ones.

In this work, we need the transmit phase data required for conductivity calculations. This data can be extracted from the measured transceive phase acquired from SE sequence [27]. This transceive phase is the signal phase received when measuring at the magnetic center of the RF pulse. In this work, the transmit phase can be approximated as half of the transceive phase [9] due to homogeneous assumption of the complex permittivity which we will discuss in the next chapter. In addition, the signal magnitude is acquired to improve phase-based conductivity reconstructions [28]. This electrical signal is caused by varying net magnetization. If the RF pulses are turned off, an alternative electric current at Larmour frequency is generated due to the precessing movement of the magnetic moment. The application and utilization of these data are explained in detail in the following chapter.

Theory & Methods

In this chapter, we will present, in detail, a theory of phase-based conductivity mapping using data from magnetic resonance imaging (MRI) apparatus with Helmholtz equation and a model-based approach with regularization proposed by Kathleen Ropella, et al. [9]. This method will be in the centre of our work, as its main purpose and goal is to create the conductivity maps using a method involving the inverse Laplacian approach which should create maps with more accuracy than with the approach that uses Helmholtz equation.

3.1 Phase-based conductivity mapping

In the highlight of the phase-based conductivity mapping is the complex permittivity which defines the electrical properties of tissue:

$$\kappa := \epsilon - i \left(\frac{\sigma}{\omega} \right), \quad (3.1)$$

where ϵ is permittivity, σ is conductivity, and ω is the resonant angular frequency introduced in section 2.2 as Larmor frequency. Here, the material's ability to conduct electric current is described by the conductivity while material's ability to resist the creation of an electric field within itself is described by permittivity.

First, by combining Faraday's and Ampere's laws from Maxwell equations, we are able to derive the following relation between the magnetic flux density, \mathbf{B} , and complex permittivity shown in the equation (3.1):

$$-\nabla^2 \mathbf{B} = \frac{\nabla \kappa}{\kappa} \times [\nabla \times \mathbf{B}] + \omega^2 \mu \kappa \mathbf{B}, \quad (3.2)$$

where ∇^2 is so-called Laplacian operator and μ is permeability which describes a material's ability to support the formation of the magnetic field within itself [9].

Here, we bring out our first assumption that will contribute to inaccuracies in our conductivity map reconstructions – we assume that the complex permittivity κ is locally constant (assumption of homogeneity). This directly results in the gradient of the complex permittivity becoming zero, and thus:

$$\frac{\nabla\kappa}{\kappa} \times [\nabla \times \mathbf{B}] = 0, \quad (3.3)$$

which, on its part, drops out the first term on the right hands side in the equation (3.2). Therefore, our now simplified equation takes the following form:

$$-\nabla^2 \mathbf{B} = \omega^2 \mu \kappa \mathbf{B}. \quad (3.4)$$

Now, we can relate the magnetic flux density to square of the complex wave number which is defined as follows [30]:

$$k^2 = \mu \epsilon \omega^2 - i \mu \sigma \omega, \quad (3.5)$$

which gives us the final Helmholtz equation:

$$\nabla^2 \mathbf{B} + k^2 \mathbf{B} = 0, \quad (3.6)$$

which is generally used to reduce the complexity of the analysis after the separation of variables in physical problems.

The Helmholtz equation can be rewritten with a harmonic magnetic field and it is valid for each Cartesian component so the magnetic field can be expressed as the effective magnetic field

$$\mathbf{B}_1^+ = (B_x + iB_y) = |\mathbf{B}_1^+| e^{i\phi^+}, \quad (3.7)$$

since this transmit radiofrequency (RF) field is used in the MRI [9,30]. Here, ϕ^+ is the phase of the \mathbf{B}_1^+ field which is affected by the conductivity of the measured object [13].

Now, we can rewrite the Helmholtz equation in (3.6) in the following form:

$$\nabla^2 \mathbf{B}_1^+ + k^2 \mathbf{B}_1^+ = 0, \quad (3.8)$$

The core idea of using the Helmholtz equation for the phase-based conductivity map reconstruction is that both magnitude of the magnetic field

and its phase are known in order to calculate the conductivity as well as permittivity of an object.

With the use of the definition of the RF field presented in the equation (3.7), we can expand the Helmholtz equation into the following form using product rule:

$$\frac{\nabla^2 B_1^+}{|B_1^+|} + \frac{2\nabla|B_1^+|\nabla e^{i\phi^+}}{|B_1^+|e^{i\phi^+}} + \frac{\nabla^2 e^{i\phi^+}}{e^{i\phi^+}} = -k^2. \quad (3.9)$$

From the definition of the squared complex wave number in the equation (3.5), it is almost trivial to specify that conductivity is in the imaginary part of it and therefore solving the conductivity is done by taking the imaginary part of the expanded Helmholtz equation in (3.9) resulting in

$$\text{Im}\left(\frac{2\nabla|B_1^+|\nabla e^{i\phi^+}}{|B_1^+|e^{i\phi^+}} + \frac{\nabla^2 e^{i\phi^+}}{e^{i\phi^+}}\right) = \sigma\mu\omega, \quad (3.10)$$

where the first term on the left hand side $\frac{\nabla^2 B_1^+}{|B_1^+|} \in \mathbb{R}$ and consequently was dropped out. In addition to the conductivity, it might be already clear that the EPT using Helmholtz equation can also compute the permittivity ϵ using a similar procedure. In order to solve the expanded Helmholtz equation (3.9) for ϵ , the real part of the equation must be taken in the similar fashion as the imaginary part, since the permittivity can be found in the real part of k^2 . However, the permittivity is not of great importance to our work and hence we will not proceed with solving the equation for ϵ .

In the continuation with the imaginary part in the equation (3.10), the first term of the left hand side is small enough in comparison to the second term for us to approximate the equation into the following form [30]:

$$\text{Im}\left(\frac{\nabla^2 e^{i\phi^+}}{e^{i\phi^+}}\right) \approx \sigma\mu\omega. \quad (3.11)$$

This approximation contributes to a relatively small error in our conductivity calculation, and we, therefore, choose to neglect it.

What is now left is the expansion of the numerator in order to write out the solution for the conductivity in as simple form as possible

$$\begin{aligned} \nabla^2 e^{i\phi^+} &= i\nabla(e^{i\phi^+}\nabla\phi^+) = i(e^{i\phi^+}\nabla^2\phi^+ + \nabla e^{i\phi^+}\nabla\phi^+) \\ &= ie^{i\phi^+}\nabla^2\phi^+ - e^{i\phi^+}(\nabla\phi^+)^2 \end{aligned} \quad (3.12)$$

where we have clear distinction between real and imaginary parts which finally allows us to write the final approximation for the conductivity:

$$\sigma \approx \frac{\nabla^2 \phi^+}{\mu_0 \omega}. \quad (3.13)$$

Here, the permeability was chosen to be a vacuum permeability as it is an acceptable approximation for the human body [30].

The result is the equation used for the phase-based conductivity mapping which is extremely time efficient since the magnitude of the field is not required at all for the computation. The transmit phase data is acquired from the spin echo (SE) sequence. This method is valid as long as the curvature of the B_1^+ field is small which increases with the strength of the static magnetic field B_0 [13].

The main issues in the Helmholtz-based EPT as well as in the EPT in general are boundary errors and low signal-to-noise ratio (SNR). The boundary errors, as the name suggests, arise at the boundaries of scanned materials due to the assumption that the permittivity is locally constant in a material while the low SNR arises from the heavy reliance on the Laplacian operator highlighted in the equation (3.2). The electrical properties of the material are proportional to the Laplacian of the magnetic fields resulting in the amplification of all types of noise produced by the MRI scan. Multiple methods have been proposed to tackle these issues including the inverse approaches into which we will dive in the following section as we present a proposed method of inverse Laplacian to create conductivity maps more accurate than those created using the Helmholtz-based EPT method [9].

3.2 Inverse Laplacian approach

In this work, we present a model-based reconstruction approach (presented by Ropella, et al. in Ref. [9]) that uses regularization in order to decrease the number of factors contributing to edge artifacts and noise amplification. In this method, inverse Laplacian, ∇^{-2} , is used for the minimization of the difference to acquired phase data from the SE scans. Apart from the transmit phase data, the method also uses information about geometry of the object to confine the calculations within a certain area by introducing boundaries using support and edge masks. The method deals with 3D maps created from the collected MRI data, so all of the data will be presented as three-dimensional tensors or as in this case, we can call them three-dimensional matrices or arrays.

The proposed method to reconstruct the conductivity map using regularized least-squares method is as follows

$$\sigma' = \operatorname{argmin}_{\sigma} \frac{1}{2} \left\| \frac{\phi^+}{\mu_0 \omega} - L\sigma \right\|_{W_1}^2 + \lambda W_2 R(\sigma), \quad (3.14)$$

where we denote the optimal conductivity with σ' , L is the matrix representation of the differential inverse Laplacian operator, ∇^{-2} , W_1 and W_2 are binary matrices used to mask out relevant areas in the reconstructed map, λ is regularization parameter, and $R(\sigma)$ is regularization function.

The first term is a quadratic function which is minimized resulting in enforced relationship between the acquired phase data and reconstructed conductivity map leading the reconstruction in the correct direction. This is done within the domain of the binary mask W_1 which will be show-cased in the more detailed optimization analysis. The second term, is the regularizing term used to minimize the rising edge artifact and to smooth the image in the area restricted and defined by the mask W_2 in the same manner as W_1 .

Before defining L , we need Laplacian operator, ∇^2 , which is defined

$$\nabla^2 = \frac{\partial^2}{\partial x^2} + \frac{\partial^2}{\partial y^2} + \frac{\partial^2}{\partial z^2}, \quad (3.15)$$

with, if we denote a 3D matrix as a function $f(x, y, z)$

$$\frac{\partial^2}{\partial x^2} f(x, y, z) = \frac{f(x - h_x, y, z) - 2f(x, y, z) + f(x + h_x, y, z)}{h_x^2}, \quad (3.16)$$

$$\frac{\partial^2}{\partial y^2} f(x, y, z) = \frac{f(x, y - h_y, z) - 2f(x, y, z) + f(x, y + h_y, z)}{h_y^2}, \quad (3.17)$$

$$\frac{\partial^2}{\partial z^2} f(x, y, z) = \frac{f(x, y, z - h_z) - 2f(x, y, z) + f(x, y, z + h_z)}{h_z^2}, \quad (3.18)$$

where $h_{x,y,z}$ are the voxel dimensions. These equations are essentially second-order central finite differences which are an approximation of the second order derivative which Laplacian operator represents in three dimensions [25]. If in the image all the voxels are identical (isotropic unit voxels) and the origin of the matrix is at its center, the resulting matrix representation of ∇^2 is $\mathbb{R}^{3 \times 3 \times 3}$ array with the following values

$$\begin{aligned} \nabla^2(0, 0, 0) &= -6, \\ \nabla^2(\pm 1, 0, 0) &= \nabla^2(0, \pm 1, 0) = \nabla^2(0, 0, \pm 1) = 1, \end{aligned}$$

$$\text{else zero.} \quad (3.19)$$

This is a representation when the voxel dimensions $h_{x,y,z} = 1$. In other cases, these resolution parameters must be added to the values of the array elements according to equations (3.16)-(3.18).

The matrix form of the inverse Laplacian, L , is first calculated by zero-padding the kernel $\nabla^2(x, y, z)$ to match the dimensions of the magnitude and phase data. Next, we take its 3D fast Fourier Transform (FFT) and invert each individual component value in the resulting matrix. However, before inverting the components, a small offset δ must be added to the zero valued DC term in the origin of the matrix in order to avoid zero division upon the inversion of the matrix components. After the offset is added and the components are inverted, we take the inverse FFT of the resulting kernel and we obtain the final form of the matrix L .

The reason this procedure is done is the fact that the inverse transform is given by the inverse of the matrix in question as shown in equation (2.13). If we invert every element of this matrix in Fourier domain, the outcome of the inverse Fourier Transform is, then, inverse of the matrix that the Fourier Transform was initially applied to.

The matrix L can be thought of as a filter and just as explained in the section 2.1.1, the filter is applied to an image or in our case, to the map using convolution. So, essentially, the $L\sigma$ representation in the equation (3.14) is the convolution operation between the two 3D arrays:

$$L\sigma := L * \sigma = \mathcal{F}^{-1}\{\mathcal{F}\{L\} \cdot \mathcal{F}\{\sigma\}\}. \quad (3.20)$$

where “ \cdot ” denotes pointwise multiplication and therefore it is important that both L and σ are of the same dimensions. Since, in the entirety of this work, we will be dealing with 3D arrays, for the sake of simplicity, we will continue using this notation in the further calculations.

The support mask W_1 is created by defining a certain threshold in the data of the magnitude of data. The values equal and above this threshold value will equal 1 while the rest will be turned to zero. This creates a binary map which will dictate the location where the reconstruction of the conductivity map will be done. The rest of the area will be neglected in the calculations due to the zero values in the mask.

The edge mask W_2 can be created using different edge detection methods and in this work we specifically used Canny edge detection operator that uses multiple stages in its algorithm [31]. This operator is applied to the magnitude map which produces a clear image of the edges of an object. These edges are then converted to zero values and the rest to equal value 1. Lastly, it is combined with W_1 mask in order to mask only the

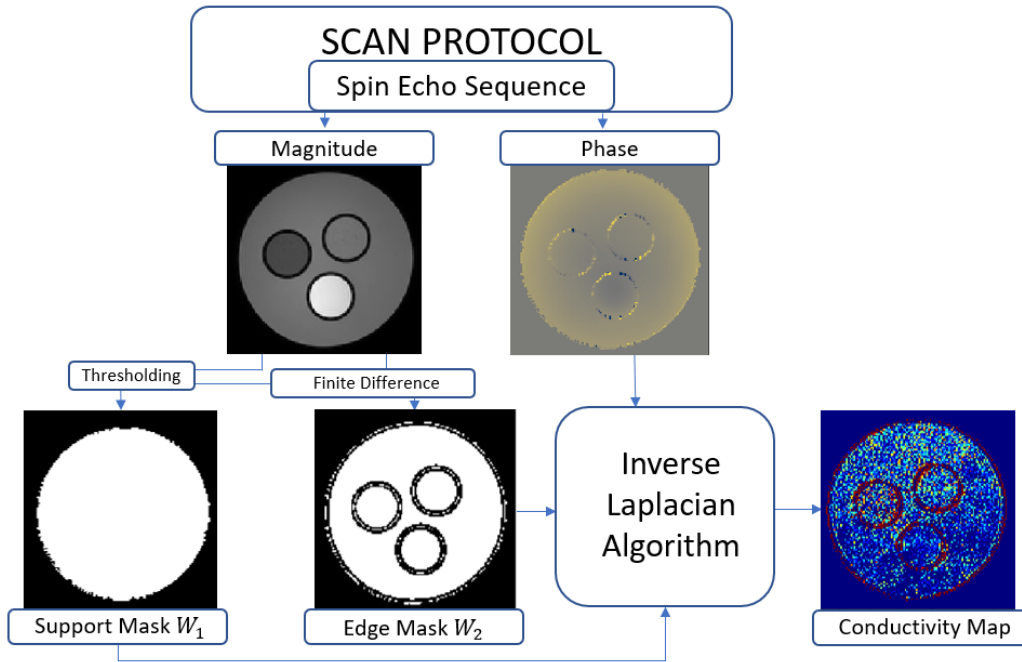


Figure 3.1: Reconstruction process from the data acquisition to conductivity map reconstruction. Phase and magnitude data are acquired from SE sequence. Masks W_1 and W_2 are obtained from geometry data and subsequently combined with phase data in IL algorithm to construct a conductivity map of the object.

object area excluding the edges within the object. The resulting mask dictates where the regularization will be applied. Examples of both W_1 and W_2 masks are shown in Figure 3.1.

The regularization function, $R(\sigma)$, consists of a squared Euclidian norm of potential function $\Psi(C\sigma)$ where C is the first order finite difference operator in the matrix form which gives out smoother conductivity map. When the regularization function is multiplied with W_2 , it calculates a weighted sum of the differences between a voxel and its adjacent neighbour in every direction.

The optimal conductivity, σ' in equation (3.14) is solved with the use of nonlinear conjugate gradient method (NCGM) [32,33,34]. This method generalizes the conjugate gradient method which solves unconstrained optimization problems such as ours with an iterative algorithm [33,34].

In order to illustrate the method in a more simplistic manner, we break the optimization problem into two cases – reconstructing the conductivity without and with the regularization term which are presented in the following sections.

3.2.1 Approach without regularization

If the regularization is not included in the reconstruction of the conductivity map, the problem reduces to

$$f(\sigma) = \frac{1}{2} \left\| \frac{\phi^+}{\mu_0 \omega} - L\sigma \right\|_{W_1}^2. \quad (3.21)$$

Since NCGM is a gradient-based method, the main idea of it is to find a local minimum of a nonlinear function using its gradient, $\nabla_{\sigma} f$, which indicates the direction of the maximum ascent. In order to show the opposite – maximum descent (or the steepest descent), simply the negative of the gradient, $-\nabla_{\sigma} f$, is taken. The form of solving the iterative optimization problem is as follows:

$$\sigma_{n+1} = \sigma_n + \alpha_n d_n, \quad (3.22)$$

where α_n is a step size which varies at each step of the iteration n and is obtained by a line search, and d_n is the search direction defined as

$$d_n = \begin{cases} -\nabla_{\sigma} f, & \text{for } n = 0; \\ -\nabla_{\sigma} f + \beta_n d_{n-1}, & \text{for } n \geq 1, \end{cases} \quad (3.23)$$

where β_n is a direction parameter (not to be confused with regularization parameter).

The algorithm itself can be broken down into five general steps:

- 1) Calculation of the steepest descent: $\Delta\sigma_n = -\nabla_{\sigma} f(\sigma_n)$,
- 2) Computation of β_n with one of the two methods shown below:

$$\beta_n^{FR} = \frac{\Delta\sigma_n^T \Delta\sigma_n}{\Delta\sigma_{n-1}^T \Delta\sigma_{n-1}},$$

$$\beta_n^{PR} = \frac{\Delta\sigma_n^T (\Delta\sigma_n - \Delta\sigma_{n-1})}{\Delta\sigma_{n-1}^T \Delta\sigma_{n-1}},$$

- 3) Update of the conjugate direction: $d_n = \Delta\sigma_n + \beta_n d_{n-1}$,
- 4) A line search: Optimization of $\alpha_n := \operatorname{argmin}_{\sigma} f(\sigma_n + \alpha d_n)$,
- 5) Update of the map: $\sigma_{n+1} = \sigma_n + \alpha_n d_n$,

where β_0 is set to zero, so that the result is correct for $n = 0$ in the equation (3.23), and σ_0 is an initial educated guess of the conductivity map.

The two formulas in the second step of the algorithm are named after Fletcher-Reeves and Polak-Ribiere methods, respectively [33,35]. Both of these formulas help the algorithm achieve the same result. However, the speed or the number of steps at which the algorithm converges may vary for these methods. In addition to the two methods presented, there are

other methods [33]. Regardless, in this work, we focus on and utilize only the two presented methods.

Some steps, namely the first and the fourth steps require more particular look into the more detailed way of computing the gradient and performing a line search, respectively.

First, the algorithm requires the gradient of our function, $\nabla_{\sigma} f(\sigma_n)$, which is the essential part of the minimization. Its calculation is fairly simple when the 3D arrays in the function are vectorized. We first expand the function, $f(\sigma)$, in the following way

$$f(\sigma_n) = \frac{1}{2} \left[\left\| \frac{\phi^+}{\mu_0 \omega} \right\|_{W_1}^2 - \left\langle \frac{\phi^+}{\mu_0 \omega}, L\sigma_n \right\rangle_{W_1} - \left\langle L\sigma_n, \frac{\phi^+}{\mu_0 \omega} \right\rangle_{W_1} + \|L\sigma_n\|_{W_1}^2 \right], \quad (3.24)$$

where due to the fact that ϕ^+ , L , and σ are real, we are allowed to exploit the commutative property

$$\left\langle \frac{\phi^+}{\mu_0 \omega}, L\sigma_n \right\rangle = \left\langle L\sigma_n, \frac{\phi^+}{\mu_0 \omega} \right\rangle, \quad (3.25)$$

which allows writing the function as

$$f(\sigma) = \frac{1}{2} \left[\left\| \frac{\phi^+}{\mu_0 \omega} \right\|_{W_1}^2 - 2 \left\langle L\sigma_n, \frac{\phi^+}{\mu_0 \omega} \right\rangle_{W_1} + \|L\sigma_n\|_{W_1}^2 \right]. \quad (3.26)$$

Now, we can take the gradient of this function resulting in

$$\begin{aligned} \nabla_{\sigma} f(\sigma_n) &= \frac{1}{2} \left[-2 \left\langle L, \frac{\phi^+}{\mu_0 \omega} \right\rangle_{W_1} + \left\langle L, L\sigma_n \right\rangle_{W_1} + \left\langle L\sigma_n, L \right\rangle_{W_1} \right] \\ &:= L \left(L\sigma_n - \frac{\phi^+}{\mu_0 \omega} \right)_{W_1}, \end{aligned} \quad (3.27)$$

where we used the property identical to the one in equation (3.25) and the final notation with reshaped matrices was written with the accordance to the rules we previously set. The reason we were able to rewrite it in the final form was due to the fact that three-dimensional maps are convoluted with the inverse Laplacian, L , which is a self-adjoint matrix. A detailed view on derivation of the gradient of the 2-norm of vector residual can be found in Appendix A.

In order to perform a line search, we need to optimize step size α in accordance to the fourth step of the algorithm. To obtain the solution for α_n , we have to solve

$$\partial_{\alpha} (\sigma_n + \alpha_n d_n) = 0. \quad (3.28)$$

Here, we use inner product also known as dot product notation which is more optimal for solving scalars. First, we expand the function as:

$$f(\sigma_n + \alpha_n d_n) = \frac{1}{2} \left\| \frac{\phi^+}{\mu_0 \omega} - L\sigma_n - L\alpha_n d_n \right\|_{W_1}^2 = \frac{1}{2} \|r_n - L\alpha_n d_n\|_{W_1}^2, \quad (3.29)$$

where $r_n = \frac{\phi^+}{\mu_0 \omega} - L\sigma_n$ denotes the residual between the phase map acquired from MRI and phase map calculated using convolution between inverse Laplacian and conductivity map of iteration step n , and α_n is a scalar. Further expansion takes form

$$f(\sigma_n + \alpha_n d_n) = \frac{1}{2} \left[\|r_n\|_{W_1}^2 - \langle r_n, \alpha_n L d_n \rangle_{W_1} - \langle \alpha_n L d_n, r_n \rangle_{W_1} + \alpha_n^2 \|L d_n\|_{W_1}^2 \right]. \quad (3.30)$$

Since we are optimizing α_n which is a scalar, we are allowed to vectorize both r_n and $L d_n$ and they both are real valued ($L, \phi^+, \sigma_n, d_n \in \mathbb{R}$). In addition, L is a self-adjoint matrix giving us the following commutative relation:

$$\alpha_n \langle r_n, L d_n \rangle = \alpha_n \langle L d_n, r_n \rangle. \quad (3.31)$$

Using the property in equation (3.31), we are finally able to write the function in (3.30) in the following form

$$f(\sigma_n + \alpha_n d_n) = \frac{1}{2} \left[\|r_n\|^2 - 2\alpha_n \langle L r_n, d_n \rangle + \alpha_n^2 \|L d_n\|^2 \right]_{W_1}, \quad (3.32)$$

where it is good to note that $L r_n$ is the gradient required for computation of the direction for the steepest descent in the first step of the algorithm. Next, we take the derivative of the function with respect to α

$$\partial_\alpha f(\sigma_n + \alpha_n d_n) = -\langle L r_n, d_n \rangle_{W_1} + \alpha_n \|L d_n\|_{W_1}^2, \quad (3.33)$$

which allows us to obtain the final formula for the optimized α

$$\alpha_n = \frac{\langle L r_n, d_n \rangle_{W_1}}{\|L d_n\|_{W_1}^2}, \quad (3.34)$$

where, dot product between $L r_n$ and d_n , and squared norm of $L d_n$ are kept within the domain of support mask W_1 .

As the final remark, we note that in order to keep the calculations and reconstruction within the desired domain, we must apply the support mask W_1 to the algorithm of the NCGM as previously stated. To do

so, we apply the mask to the initial form of the conductivity σ_0 in equation (3.22) using pointwise multiplication. In next steps of the iteration process, we apply the mask only to the gradient of the entire function in the similar fashion. Since the outcome of every step of the algorithm depends on the gradient, the effect of the application of the mask will automatically transfer to the outcomes of these steps as shown in derivations above. Hence the mask is applied only once which significantly reduces the computation complexity of the algorithm.

3.2.2 Approach with regularization

Upon having the regularization term in equation (3.14), adding the regularization to the algorithm is not as difficult of a task as might seem at first. The only parts of the algorithm that need to be modified are the first and the fourth steps which were inspected closely in the previous section. The regularizing term is added to the data term, minimum of which the algorithm strives to find. This means that we do not need to perform the calculations for the gradient and the step size from the very beginning. Instead, we can take readily calculated parts from the data term in the previous section and add differentiated terms to it.

Before presenting formulas for the gradient of the function and the step size, we define the regularization function

$$R(\sigma) = \|A\sigma\|_{W_2}^2, \quad (3.35)$$

where the use of such regularization function is called Tikhonov's regularization. The first finite difference operator, A , is picked to be suitable regularization matrix [34]. This way, values of the regularization function grow in the manner of a quadratic function which allows to penalize the roughness in the conductivity map in nonlinear fashion [9]. Depending on the data and the object we are dealing with, occasionally Laplacian (second order finite difference) can also be used as the regularization matrix. However, it is of great rarity that Laplacian produces better results than the first order finite difference operators [36].

Matrix form of the first finite difference operator, A , is constructed the same way as the Laplacian operator in the previous section. Only this time, we follow the rules of operators introduced in Chapter 2 in equations (2.20)-(2.22). The three finite difference operators take the following matrix forms:

Central finite difference:

$$C(\pm 1, 0, 0) = C(0, \pm 1, 0) = C(0, 0, \pm 1) = \pm 1,$$

$$\text{else zero,} \quad (3.36)$$

Forward finite difference:

$$\begin{aligned} F(0,0,0) &= -3 \\ F(1,0,0) &= F(0,1,0) = F(0,0,1) = 1, \\ &\text{else zero,} \end{aligned} \quad (3.37)$$

Backward finite difference:

$$\begin{aligned} B(0,0,0) &= 3 \\ B(-1,0,0) &= B(0,-1,0) = B(0,0,-1) = -1, \\ &\text{else zero.} \end{aligned} \quad (3.38)$$

Essentially, we use these matrices as any other operator in this work by convoluting them together with our 3D maps representation of which is shown in equation (3.20). However, these finite difference operators are not self-adjoint matrices forcing us to define their adjoints separately in our calculations.

Now, we compute the gradient of the function with the regularization. We take the calculated gradient from the equation (3.27) and add the gradient of the regularization term to it

$$\begin{aligned} \nabla_{\sigma} f(\sigma_n) &= L \left(\frac{\phi^+}{\mu_0 \omega} - L\sigma_n \right)_{W_1} + \lambda \nabla_{\sigma} (\|A\sigma_n\|_{W_2}^2) \\ &= L \left(\frac{\phi^+}{\mu_0 \omega} - L\sigma_n \right)_{W_1} + \lambda W_2 \text{adj}(A)(A\sigma_n), \end{aligned} \quad (3.39)$$

where $\text{adj}(A)$ is adjoint of A which in three dimensional case does not equal the transpose of A unlike in two-dimensional case.

Computing the step size can be done in the similar manner by taking already existing calculations from the equation (3.32), adding the regularization term to it, and expanding it

$$\begin{aligned} f(\sigma_n + \alpha_n d_n) &= \frac{1}{2} \left[\|r_n\|_{W_1}^2 - 2\alpha_n \langle Lr_n, d_n \rangle_{W_1} + \alpha_n^2 \|Ld_n\|_{W_1}^2 \right]_{W_1} \\ &\quad + \lambda \|A(\sigma_n + \alpha_n d_n)\|_{W_2}^2 \\ &= \frac{1}{2} \left[\|r_n\|_{W_1}^2 - 2\alpha_n \langle Lr_n, d_n \rangle_{W_1} + \alpha_n^2 \|Ld_n\|_{W_1}^2 \right] \end{aligned}$$

$$+ \lambda \left(\|A\sigma_n\|_{W_2}^2 + \alpha_n \langle A\sigma_n, Ad_n \rangle_{W_2} + \alpha_n \langle Ad_n, A\sigma_n \rangle_{W_2} + \alpha_n^2 \|Ad_n\|_{W_2}^2 \right), \quad (3.40)$$

where $r_n = \frac{\phi^+}{\mu_0\omega} - L\sigma_n$ is the residual. Next, we take the derivative of the function with respect to α

$$\begin{aligned} \partial_\alpha f(\sigma_n + \alpha_n d_n) &= -\langle Lr_n, d_n \rangle_{W_1} + \alpha_n \|Ld_n\|_{W_1}^2 \\ &+ \lambda \left(\langle A\sigma_n, Ad_n \rangle_{W_2} + \langle Ad_n, A\sigma_n \rangle_{W_2} + 2\alpha_n \|Ad_n\|_{W_2}^2 \right). \end{aligned} \quad (3.41)$$

Unlike in the case with Laplacian, the finite difference operator is not self-adjoint,

$$\langle A\sigma_n, Ad_n \rangle \neq \langle Ad_n, A\sigma_n \rangle, \quad (3.42)$$

and therefore equation (3.41) remains unchanged. The final stage of optimization is done by solving step size, α , from $\partial_\alpha f(\sigma_n + \alpha_n d_n) = 0$

$$\alpha_n = \frac{\langle Lr_n, d_n \rangle_{W_1} - \lambda \left(\langle A\sigma_n, Ad_n \rangle_{W_2} + \langle Ad_n, A\sigma_n \rangle_{W_2} \right)}{\|Ld_n\|_{W_1}^2 + 2\lambda \|Ad_n\|_{W_2}^2}. \quad (3.43)$$

We see that the only difference to the corresponding step size for the case without regularization in equation (3.34) is a subtracted term in the numerator and an added term in the denominator. This allows the compensation of the step size with different regularization parameter values as the step size becomes inversely proportional to the parameter which, in principle, avoids the errors in each step size of the iteration.

Results & Discussion

In this chapter, we will present our results of conductivity map reconstructions introduced and discussed in Chapter 3. Apart from demonstrating the reconstruction for both cases: without and with regularization, respectively, we will show different ways of determining parameters needed in the algorithm along with functionality and practicalities of the algorithm itself. We perform first analysis on simulated data where real conductivity of an object is known in order to estimate the accuracy of the reconstructed conductivity values before moving onto experimental data.

4.1 Approach without regularization

The conductivity map of the simulated object can be found on the left hand side of Figure 4.1 and the map on the right side displays the outcome of the time efficient Helmholtz-based conductivity reconstruction of equation (3.13) where we convolute Laplacian with acquired phase data. We show central slices of the reconstructed maps in order to demonstrate the results in two dimensions.

As can be clearly seen, the Helmholtz-based approach produces a map of the object with fairly accurate geometry with moderate inaccuracies in conductivity values and edge artifacts arising in places where sharp transitions between the conductivity values occur. Like mentioned before, these edge artifacts arise from the assumption that the complex permittivity is locally constant. In addition, ringing effect can be observed within the outer tubes by visual analysis while small oscillations in data values can be observed within the inner tubes as well. This is called the Gibbs Phenomenon. It arises due to the fact that we are using the convolution

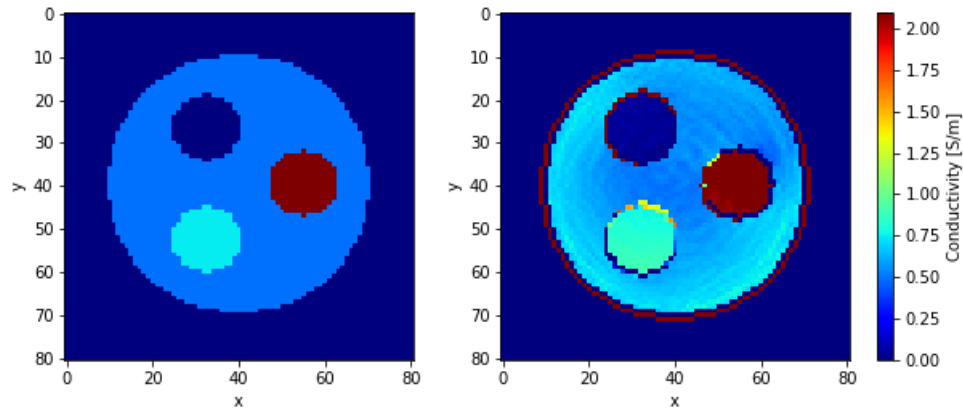


Figure 4.1: Conductivity maps for the simulated data. First image is real conductivity of the simulated object and the second is reconstruction using Helmholtz-based EPT. X and Y -axes indicate number of pixels in proprietary direction. Colour scale indicates the intensity of the conductivity values in siemens per meter.

theorem introduced in section 2.1.3 where the Fourier series on piecewise differentiable function starts behaving peculiarly as it sums overshoot at sharp transitions in values. The series has high oscillations at the sharp edges which do not die out when more terms are added to the overshoot and hence we see the boundary artifacts [37]. The ringing within the inner tubes remains due to the fact that the number of added terms is finite and therefore the values between higher edge transitions remain oscillatory. We will observe the SNR later on in this chapter as initially we did not add noise to the phase data used for the reconstruction.

We start our reconstructions with initial phase data from the simulation without the regularization term. We kept the data noise free in order to observe possible benefits of the inverse Laplacian approach for the comparison to the direct Helmholtz approach before diving into the smoothing abilities of the regularizer.

As the first step, in order to determine useful offset δ for the DC coefficient of the inverse Laplacian to avoid the division by zero, we tested the algorithm with a range of offset values $\delta = [10^{-1}, 10^4]$. The results with different offset values are displayed in Figure 4.2 for a certain number of iterations with each value. For $\delta = 10^{-1}$, the conductivity map is severely underdeveloped displaying large fluctuations in form of rings in values across the entire domain of W_1 mask with high values spread out across and beyond the boundary artifacts. For $\delta = 10^0$ and $\delta = 10^1$, noticeable cross hatching is present close to the edges of W_1 mask domain. Offset

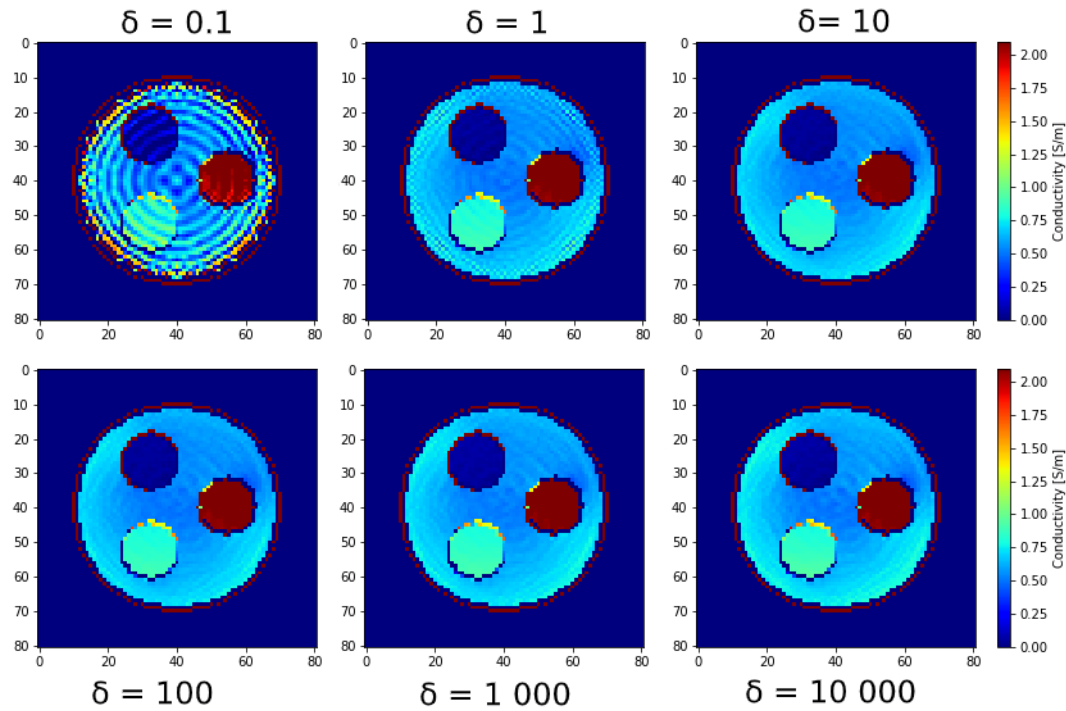


Figure 4.2: Conductivity maps reconstructed using the inverse Laplacian approach with different δ offset values added to the DC coefficient without regularization. δ was varied between values 10^{-1} and 10^4 . Every reconstruction was run over the same number of iteration steps.

$\delta = 10^2$ seems to have the closest values to those of the map reconstructed using the Helmholtz EPT equation while $\delta = 10^3$ and $\delta = 10^4$ have increase in the conductivity values close to the edges of the outer tube. We, henceforth, conclude that the most reliable offset value is around $\delta = 100$ and continue performing further experiments using this value.

Throughout our experiments, we noticed that δ value is dependent on the size of the object as well as the dimensions of the voxels i.e. the resolution of the image. Therefore, it should be possible to determine a suitable offset value using these parameters. However, as of the moment this work is written, we have not focused on determining the optimal δ value by any other than experimental means.

In Figure 4.3, we display the progress of the reconstruction using the offset value $\delta = 10^2$ at different number iterations until the minimization converged. We clearly see the effect of Gibbs ringing present in the early stages of the reconstruction. First, rings with extremely high and low values begin to form. Then, as more terms are added to the reconstruction

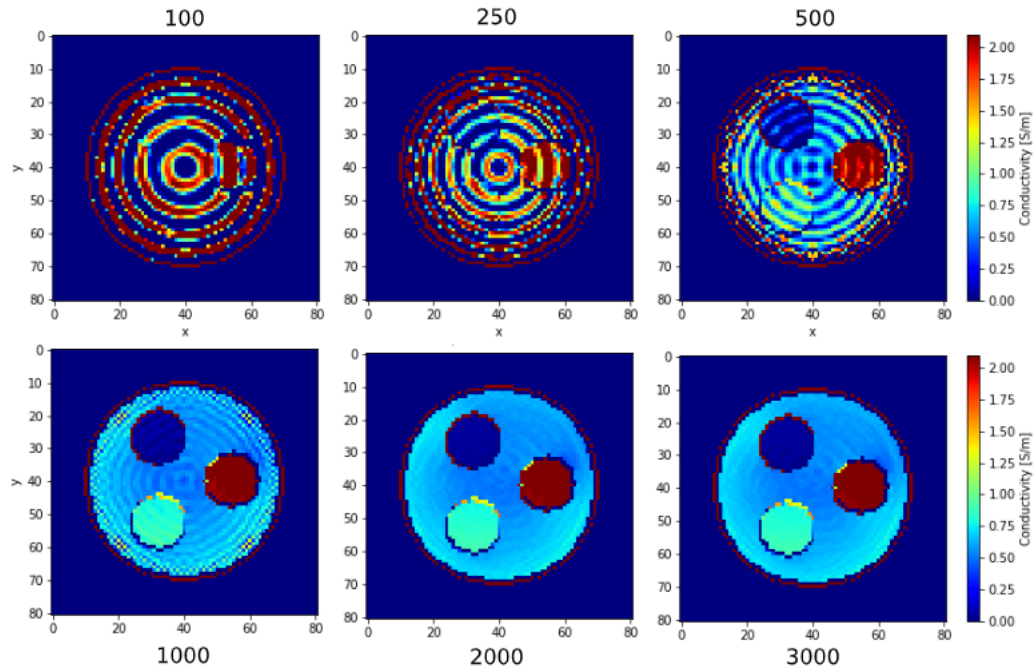


Figure 4.3: Reconstruction of the conductivity map with the initial guess of a map with nothing but zero values with $\delta = 10^2$ used for the inverse Laplacian. The observations were made after 100, 250, 500, 1000, 2000 and 3000 iterations. In this case, the number of iteration needed before the reconstruction converged was approximately 3000.

with the number of iterations, the sharp edges between the rings start decreasing and finally converge to nearly identical values. However, when the minimization converges, some ringing is still present due to the fact that the added terms do not kill the overshoot produced by the Fourier series as described by the Gibbs phenomenon [37].

In Figure 4.4, we display a normalized cost function which is representation of functional convergence as a function of number of iteration steps during this reconstruction. The functional is simply a squared Euclidian norm of the residual between initial phase data and reconstructed phase map by applying inverse Laplacian to conductivity map within the W_1 domain:

$$F(\sigma) = \left\| \frac{\phi^+}{\mu_0 \omega} - L\sigma \right\|_{W_1}^2 \quad (4.1)$$

We see a huge drop within 250 iterations which makes sense since the reconstructions started from a zero-valued conductivity map. Past the point of 250 iterations, the algorithm mainly works on equalising the difference

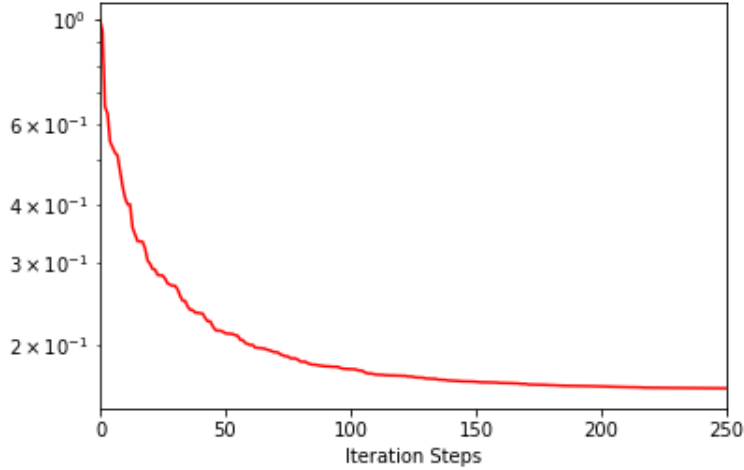


Figure 4.4: Normalized cost function of the reconstruction for 250 iteration steps. Here the functional values are displayed as a function of number of iteration steps.

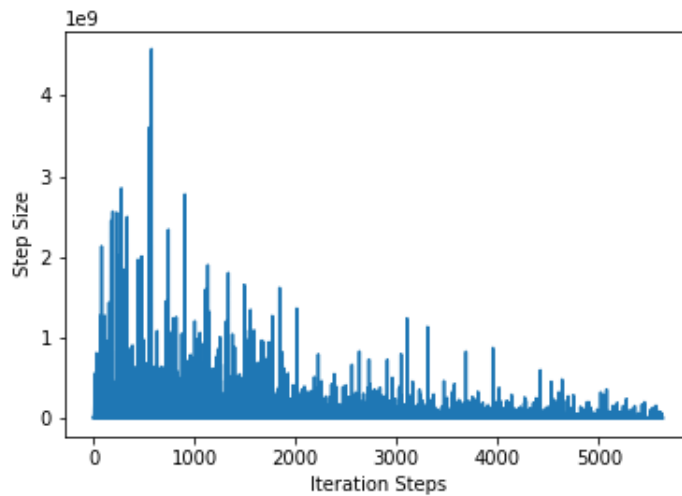


Figure 4.5: Step sizes as a function of number of iteration steps. Step size converges to nearly zero for the large number of iteration steps.

between the rings resulting in a smaller drop of the cost function. This highlights the fact that the sequence is monotonic [38]:

$$F(\sigma_0) \geq F(\sigma_1) \geq \dots \geq F(\sigma_n) \quad (4.2)$$

i.e. the value of the cost function consistently decreases with the number

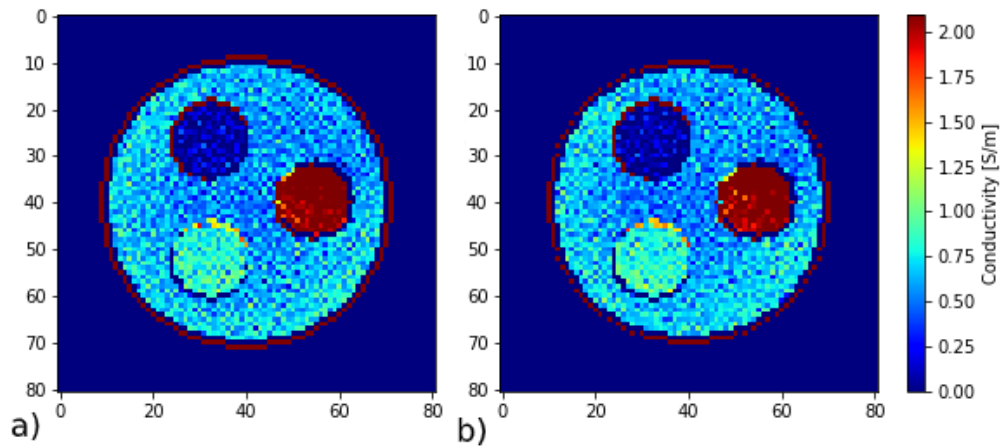


Figure 4.6: Comparison between conductivity maps reconstructed using Helmholtz EPT and inverse Laplacian approach with added noise making SNR=100. (a) Helmholtz EPT (b) Inverse Laplacian approach.

of iteration steps which indicates that we are moving steadily towards the local minimum of the functional. Since in our case we have a quadratic function, it has only one minimum which is the global minimum of the minimization problem. The step size as a function of iteration steps in Figure 4.5 further confirms the convergence as it reduces to nearly zero for a large number of iterations.

As the final analysis for the reconstruction without the regularization applied to the conductivity, we add the noise to the initial phase data of the simulation and compare the differences between SNR for both the Helmholtz EPT and the inverse Laplacian approach. The noise we add is additive white Gaussian noise (AWGN) to the imaginary part of the field magnitude with mean value set to 10^{-8} and standard deviation set to 10^{-10} making SNR = 100. The results are displayed in Figure 4.6.

The difference between the two methods of reconstruction are nearly identical with some exceptions in form of higher noise values close to the edge of the tubes in the inverse approach. The reconstruction using the unregularized inverse Laplacian approach does not get rid of the noise at all and reconstructs the image preserving nearly identical SNR to the one in Helmholtz EPT. Occasional local noise that is higher in the Inverse Laplacian approach could possibly correspond to the fact that noise can be amplified even further due to the added terms with amplified noise in the Fourier series in the reconstruction.

With these arguments, we conclude that the conductivity reconstruc-

tions obtained using the unregularized inverse Laplacian based method correspond to the those obtained via conventional deconvolution using the Laplacian kernel. This is in line with the mathematical formulation, as no additional constraints or a priori information has been incorporated. In addition, the unregularized method is more time consuming than the conventional method.

4.2 Approach with regularization

4.2.1 Simulated data

In this section, we use the same method of reconstruction as in the previous section, except now we add the regularization term into our functional:

$$F(\sigma) = \left\| \frac{\phi^+}{\mu_0 \omega} - L\sigma \right\|_{W_1}^2 + \lambda \left\| A\sigma \right\|_{W_2}^2. \quad (4.3)$$

We first look at the results in this approach using four different finite difference operators A – Laplacian i.e. second order finite difference, and first order Forward, Backward, and Central finite difference operators. We add complex white Gaussian noise to the input data making $\text{SNR} = 100$ and compare the results among each other and to the Helmholtz EPT reconstruction. We show the difference between the reconstruction using only the support mask W_1 defining the object domain, and using both the support mask W_1 , and the edge mask W_2 which delimits inner tubes from the general domain. Finally, we compare the approach with regularization to Helmholtz EPT with applied Gaussian filter to determine whether the inverse approach with regularization has any advantages over the Helmholtz EPT.

In order to reconstruct the conductivity map with regularization penalty from any desired initial guess, a right regularization parameter λ must be selected. It determines the balance between the term that models accurate data and the smoothing regularization term. While, different ways of choosing an optimal value for λ exist [9], we set $\lambda = 0.1$ and performed regularization on the initial guess corresponding to the outcome of the Helmholtz EPT.

Since, the gradients in the approach with regularization require additional adjoint operators for Forward, Backward, and Central finite difference operators involved in the regularization term of the cost function, we determine them in the following way:

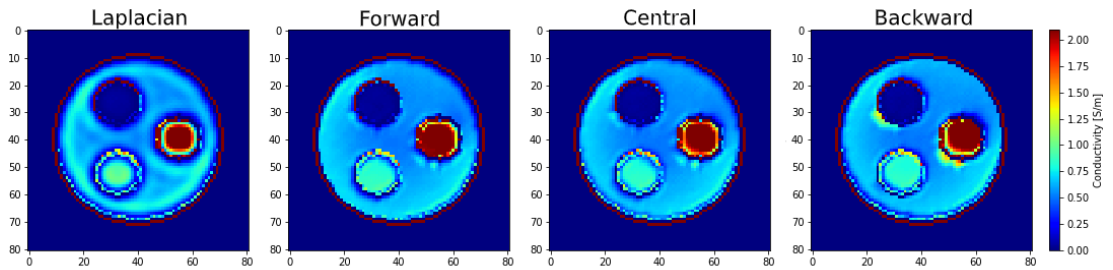


Figure 4.7: Conductivity reconstruction using Laplacian operator and Forward, Central, and Backward finite difference operators in the inverse Laplacian approach with regularization on data with SNR = 100.

Adjoint matrix to Forward finite difference:

$$\begin{aligned} \text{adj}(F)(0,0,0) &= -3 \\ \text{adj}(F)(-1,0,0) &= \text{adj}(F)(0,-1,0) = \text{adj}(F)(0,0,-1) = 1, \\ &\text{else zero,} \end{aligned} \tag{4.4}$$

Adjoint matrix to Backward finite difference:

$$\begin{aligned} \text{adj}(B)(0,0,0) &= 3 \\ \text{adj}(B)(1,0,0) &= \text{adj}(B)(0,1,0) = \text{adj}(B)(0,0,1) = -1, \\ &\text{else zero.} \end{aligned} \tag{4.5}$$

However, as the adjoint operator to Central finite difference operator turned out not to be trivial to obtain, we used forward differencing at every odd iteration step and backward differencing at every even number of steps. This should, in principle, operate in the same fashion as the central differencing. This can be seen from a sum of forward and backward differences in equations (2.21)-(2.22) resulting in central difference. Hence, we will keep referring to this operation as central differencing. The Laplacian is a self-adjoint matrix so it does not require separate specification concerning the adjoint matrix.

Results of the conductivity maps using the four operators in the regularizer can be found in Figure 4.7. Using the Laplacian operator as regularization matrix somewhat smooths the map equally in every direction. However, it produces severe ringing effect in areas close to the edges set by the edge mask W_2 and does not seem to be able to equalize them. This

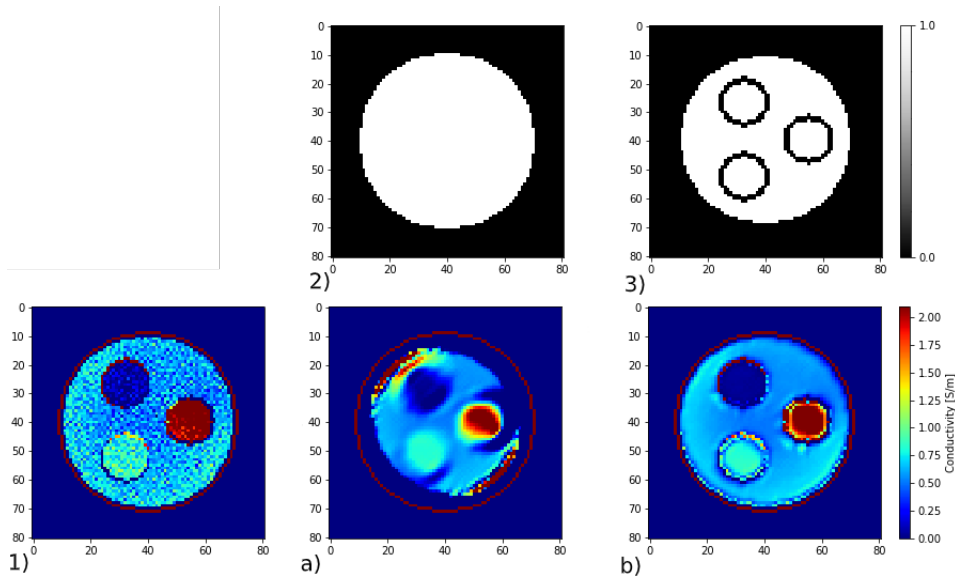


Figure 4.8: The effects of the regularization using Central finite difference operator with application of different masks. (1) Reconstruction without regularization with $\text{SNR} = 100$ (2) W_1 mask (3) W_2 mask (a) Regularization with only W_1 mask (b) regularization with both W_1 and W_2 masks.

is due to the second order derivative approximation that Laplacian represents which, in general, is less accurate than first order derivative approximation that the rest of the operators correspond to. The rest of the operators indeed do not produce such a severe ringing effect at the boundaries of the edge mask and instead improve the overall uniformity of the reconstructed conductivity. We see that the main areas within the tubes are smoothed nicely excluding small areas at the boundaries of the inner cylinders. Forward difference produces the smoothing in one direction which is the lower left corner of the map. Backward difference operates in the similar fashion with the only difference being the inclination into the opposite direction. These effects result in small imbalance within the tubes with the edges in the direction of the operators obtaining conductivity values with more accuracy than the edges on the opposite sides. On its part, the central difference operates as a middle ground between forward and backward operators. It smoothens areas evenly without emphasis in one of the directions and produces slight inaccuracies along the sharp transition edges in values.

The differences in the results between these operators could potentially be exploited. For instance, if an area of an object that one wants to focus on is known, the difference operator can be chosen in such a way that the

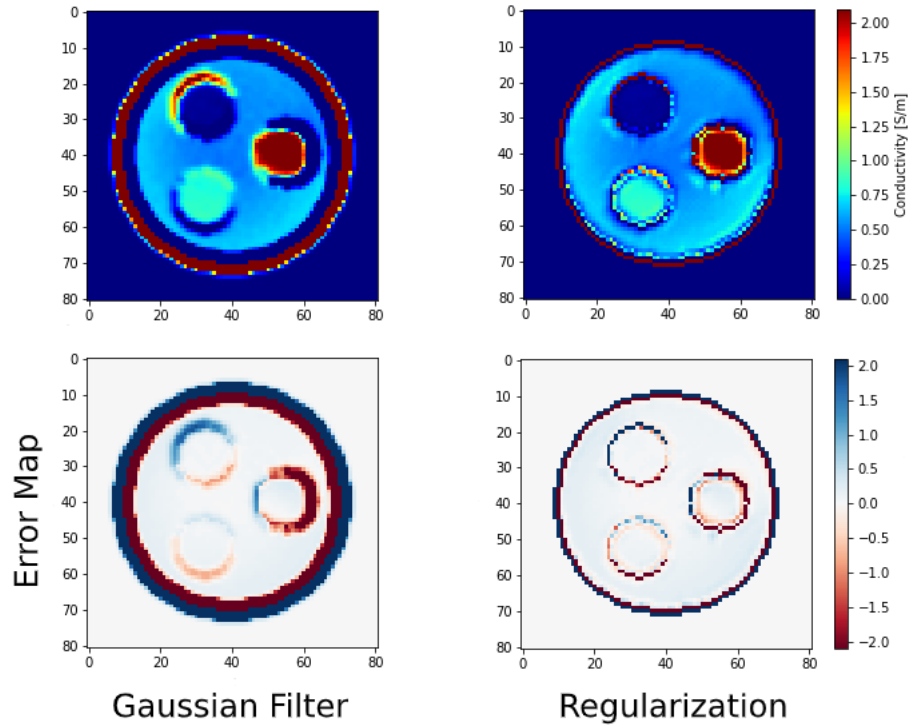


Figure 4.9: Comparison between Gaussian filter and smoothing using inverse Laplacian approach with regularization with Central finite difference operator. Error maps between reconstructed conductivity and real conductivity are displayed below. These maps confirm that the inverse approach with regularization reconstructs maps with higher accuracy than Helmholtz EPT.

shift in the accuracy is directed into the desired location.

In order to showcase the importance of the edge mask in the regularization, we show the effect of the smoothing solely by using threshold mask W_1 and by applying both W_1 and W_2 masks. We choose Central finite difference operator for this comparison. The comparison is displayed in Figure 4.8.

As one can see, without the use of the edge mask W_2 that would set boundaries at the edges of the tubes, the difference is also taken with values outside the object resulting in the wrong values washing into the domain of the object as well as the inner tubes. This is precisely what the edge mask was designed to prevent. We can see when the mask is applied to the regularization, it preserves the conductivity values near the edges by preventing the differential operation from applying on the sharp transitions in conductivity values.

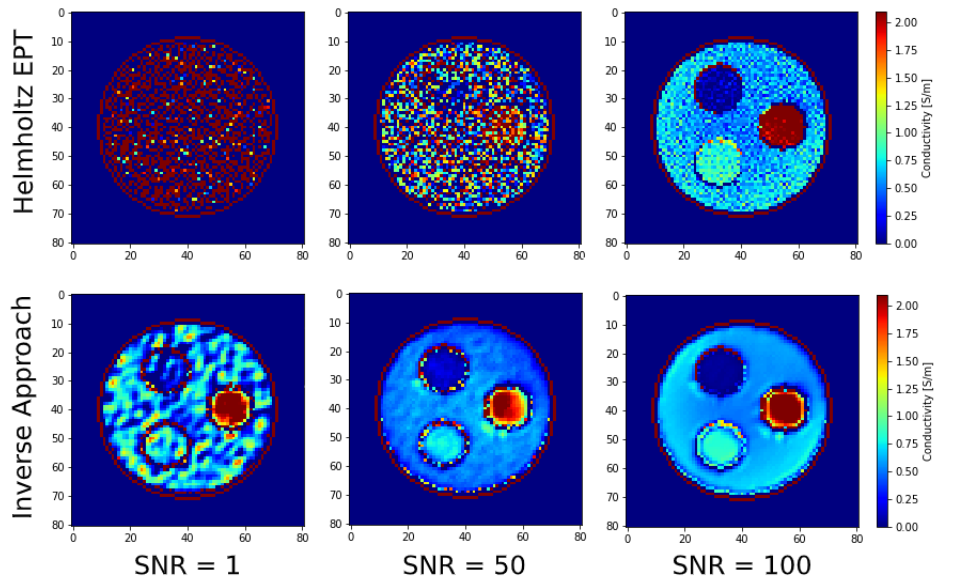


Figure 4.10: Comparison between direct Helmholtz EPT conductivity map reconstruction and inverse Laplacian approach with data with three different SNR levels.

Finally, we compare the results from the penalized regularization using Central difference operator to smoothed outcome of the Helmholtz EPT with Gaussian filter with standard deviation set to one [39]. In addition, we demonstrate the amount of difference between the reconstruction and the real conductivity displayed in the beginning of the chapter. The comparison is found in Figure 4.9.

We observe that Gaussian filter smooths the conductivity values more evenly in the areas where conductivity values are supposed to be constant.

However, these values are higher in the comparison to the real conductivity and additionally it creates enormous voids and overshoots at the sharp transition jumps resulting in more inaccuracies than the regularization especially since these voids in parts overlap with the inner tube hence removing parts of possibly desired object.

We, therefore, conclude that the inverse Laplacian method has advantages over the Helmholtz EPT with Gaussian filter mainly by producing clearer and more accurate smoothed conductivity maps using noisy data. This is significant advantage especially with data with relatively poor SNR. In addition, data from MRI always possesses noise coming from the background signal produced by the air surrounding the object [40]. In order to increase the SNR in MRI, the averaging and more phase

steps are required which take notable amount of time [40]. For this reason alone, the MRI acquisition time increases significantly in order to increase the SNR. By applying the inverse Laplacian approach to the data with relatively low SNR, the acquisition time from MRI and reconstruction time of more accurate conductivity maps are reduced. This is due to the fact that if the initial guess in the inverse approach is a map from Helmholtz EPT, the algorithm reaches the convergence point within 100 iterations which takes 1 – 30 seconds depending on the size of the input data and the resolution of reasonably sized objects.

To further confirm these observations, we compare the results between the outcome of the Helmholtz EPT and the inverse approach with regularization on the same data with three levels of SNR: 1, 50, and 100. The comparison is found in Figure 4.10.

In the future, an optimal method to choose the correct regularization parameter λ could be implemented which would allow the reconstruction of the maps with regularization from any arbitrary initial guess. On average, throughout this work, the reconstructions with arbitrary initial guesses reached the point of convergence within 5 – 10 minutes, again, depending on the size of the input phase data and image resolution. This shows that more accurate maps can be acquired faster with regularized inverse approach than using the additional MRI scans.

4.2.2 Phantom data

In addition to simulated data, we also run the algorithm on data from two different scans on the same phantom. Table 4.1 provides important characteristics of the phantom made and extracted from Ref. [41]. For us, the most important information are the variations in conductivity between the tubes which are measured to be between 0.11 – 2.24 S/m.

Cylinder phantom	Target		Recipe				Measured	
	σ [S/m]	ϵ_r	H ₂ O [mL]	Agarose [g]	NaCl [g]	PVP [g]	σ [S/m]	ϵ_r
Tube 1	0	40	100	0.3	0	117.7	0.11	37.3
Tube 2	0.75	40	100	0.4	7	117.7	-	-
Tube 3	2.1	79.5	100	0.3	1.32	0	2.24	70.3

Table 4.1: Recipes used for the fabrication of the cylindrical phantom extracted from Ref. [41]. Important information for our experiments is contained within the measured conductivity data.

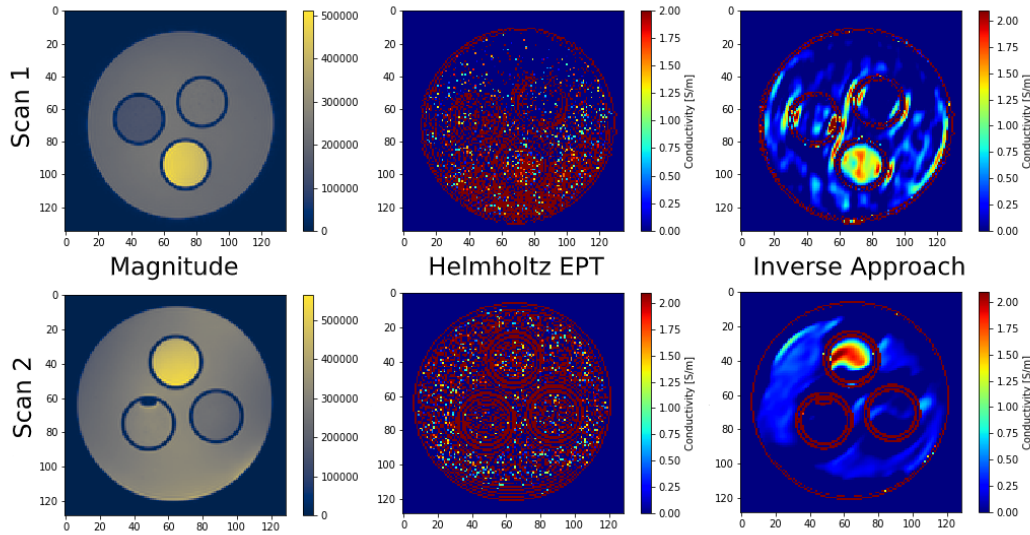


Figure 4.11: Results of the conductivity map reconstructions using Helmholtz EPT and Inverse Laplacian approach with data from two different phantom scans. Scan 1 is multi-slice turbo spin-echo scan and Scan 2 is balanced steady state free precession scan.

The first scan was multi-slice turbo spin-echo scan (MSTSE) while the second was balanced steady state free precession scan (BSSFP).

Figure 4.11 shows a comparison of the results between Helmholtz EPT and the inverse approach with regularization with the data from the two scans. We first display the images of the MRI signal magnitude to show the geometry of the phantom and the location of the inner tubes. In addition, we see the magnitude of the signal which, in principle, should be proportional to the conductivity of the object.

We see that the Helmholtz EPT produces extremely noisy and unresolvable conductivity maps where only the geometries of the phantom can be resolved. On the contrary, we see that the inverse Laplacian approach produces smoothed images, confining the different conductivity values within defined regions of the edge mask W_2 , proving its functionality. Interestingly, we see clear variations between the desired conductivity values in the outcomes of both scans although the outcome of the data from the second scan is more evenly smoothed. As a down side, we see that in the second scan, the conductivity values do obtain significant errors close to the edges of the tubes.

Nonetheless, we noticed that these boundary errors are dependent on

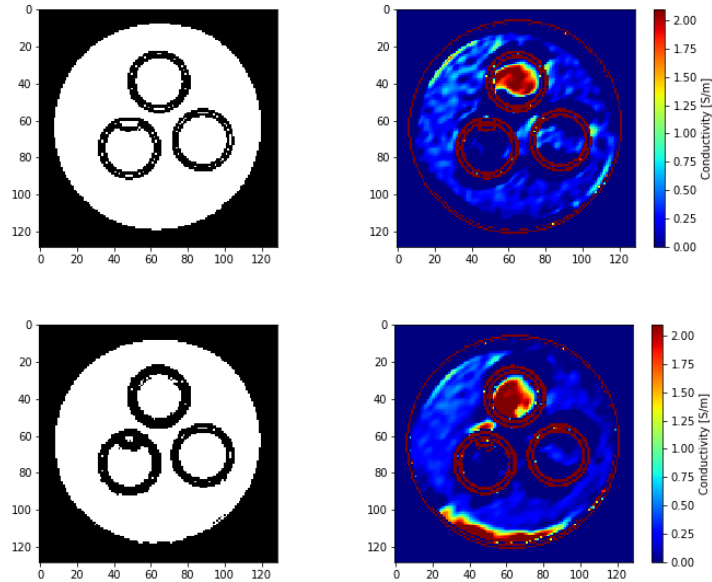


Figure 4.12: Comparison of reconstructed conductivity maps using different edge masks.

how the edge mask is defined. Comparison of the conductivity reconstruction with two different edge masks is displayed in Figure 4.12.

We see that when the edges of the inner tubes of the edge mask are more robustly defined, the correct conductivity values spread out more evenly across the confined areas of the tubes. However, as a trade off, we observe a rising boundary artifact at the bottom of the map. As of the moment of this thesis, we are not certain what causes this artifact to emerge.

Although we present only the center slices of our obtained maps, the conductivity values do not vary significantly as we inspect other slices while moving away from the center.

These observations confirm that the algorithm of regularized inverse Laplacian approach also works on acquired MRI data with phantoms. In addition, it produces conductivity maps which are more accurate and robust than those of the Helmholtz EPT. However, dependence of the accuracy of the conductivity on the edge mask was observed which may require further inspection in the future.

Conclusion

In conclusion, we successfully created an optimized phase-based conductivity map reconstruction algorithm for cases with and without regularization using inverse Laplacian approach. Successful results were demonstrated with both simulated as well as phantom data. For the optimization, we used nonlinear conjugate gradient method which exploited only the gradient of the nonlinear quadratic function to find its global minimum. For the case with added regularization term, we utilized standard Tikhonov's regularization method using approximation of a gradient or Laplacian operator as suitable regularization matrix operating on reconstructed conductivity maps. With the help of correctly constructed threshold and edge masks, we managed to constrain the regularization within the object's boundaries fairly accurately in contrast to the effects of Gaussian filter on the reconstructed maps.

However, we observed that the inverse approach without regularization does not have any advantages over direct Helmholtz-based method as both methods produced nearly identical conductivity maps without having any effect on the edge artifacts nor on the noise in the data. In some parts, the inverse approach even seemed to amplify the noise and as it is more time consuming being an iterative method, it was deemed of no use without regularization.

Nonetheless, the approach presented promising advantages over the direct method as long as the regularization was implemented. It clearly smoothed out noise within the areas dictated by the auxiliary masks more accurately than the Gaussian filter used for the comparison. It also posed advantages in the acquisition time as regularization was able to handle and smooth out maps with relatively low SNR values. This promises great advancement as the longer scan would not be needed in order to in-

crease the SNR of the reconstructed images. In addition, the algorithm was relatively fast, taking only 1 – 30 seconds to smooth maps with initial step set from product of the direct method and 5 – 10 minutes if the initial guess was completely arbitrary. Another possible exploitable perk was the use of different regularization matrices which produced higher accuracies in the reconstructed maps depending on their operation directions which could be easily modified. This would allow the observation of desired areas in inspected object to be more accurately observable in cases where the location of the desired artifact was known.

In the future, an optimal selection of regularization parameter could be implemented so that it would pose a constant balance between the optimization and the regularization terms throughout the iteration process. This would allow the regularized reconstructions from any arbitrary initial guesses. In addition to optimizing the parameter, other, perhaps, more accurate methods for regularization could be implemented. Some of them are discussed in Ref. [42]. These methods could possibly modify the penalty functions dictating the amount of the regularization depending on the severity of the transition in data values due to the noise. This would allow even more precise smoothing close to the edges of the reconstructed objects and faster smoothing in general than the quadratic regularization function used in Tikhonov's method. Furthermore, the homogeneous assumption of complex permittivity could be avoided which would, perhaps, require numerical simulations to find a solution for conductivity in order to implement it into the inverse Laplacian approach and further improve the accuracy of the results.

Due to the promising results of the algorithm used with phantom data, we are expecting that similar results with in-vivo data can be achieved.

Bibliography

- [1] Pohost, G. H., Elgavish, G. A., & Evanochko, W. T., [Nuclear Magnetic Resonance Imaging: With or Without Nuclear?](#), *JACC*, **7** (3): 709-710 (1986)
- [2] Rabi, I. I., & Breit, G., [On the interpretation of present values of nuclear moments](#), *Physical Review*, **46**: 230-231 (2018)
- [3] Foster, K. R., & Schwan, H. P., [Dielectric properties of tissues and biological materials: a critical review](#), *Critical Reviews in Biomedical Engineering*, **17** (1): 25-104 (1989)
- [4] Hancu, I., Liu, J., Hua, Y., & Lee, S. K., [Electrical properties tomography: Available contrast and reconstruction capabilities](#), *Magnetic Resonance in Medicine*, **81** (2): 803-810 (2018)
- [5] Haacke, E. M., Petropoulos, L. S., Nilges, E. W., & Wu, D. H., [Extraction of conductivity and permittivity using magnetic resonance imaging](#), *Physics in Medicine & Biology*, **36** (6): 723 (1991)
- [6] Katscher, U., Voigt, T., Findeklee, C., Vernickel, P., Nehrke, K., & Dössel, O., [Determination of electric conductivity and local SAR via B1 mapping](#), *IEEE Trans Med Imaging*, **28** (9): 1365-1374 (2009)
- [7] van Lier, A. L. H. M. W., Raaijmakers, A., Voigt, T., Lagendijk, J. J. W., Luijten, P. R., Katscher, U., & van den Berg, C. A. T., [Electrical Properties Tomography in the Human Brain at 1.5, 3, and 7T: A Comparison Study](#), *Magnetic Resonance in Imaging*, **71** (1): 354-363 (2013)
- [8] Zhang, X., Zhu, S., & He, B., [Imaging electric properties of biological tissues by RF field mapping in MRI](#), *IEEE Trans Med Imaging*, **29** (2): 474-481 (2010)

-
- [9] Ropella, K. M., & Noll, D. C., [A Regularized, Model-Based Approach to Phase-Based Conductivity Mapping Using MRI](#), *Magnetic Resonance in Medicine*, **78** (5): 2011-2021 (2016)
- [10] Miranda, P. C., Hallett, M., & Basser, P. J., [The electric field induced in the brain by magnetic stimulation: a 3-D finite-element analysis of the effect of tissue heterogeneity and anisotropy](#), *IEEE Trans Biomed Eng*, **50** (9): 1074-1085 (2003)
- [11] Wagner, T. A., Zahn, M., Grodzinsky, A. J., & Pascual-Leone, A., [Three-dimensional head model simulation of transcranial magnetic stimulation](#), *IEEE Trans Biomed Eng*, **51** (9): 1586-1598 (2004)
- [12] Wagner, T., Fregni, F., Fecteau, S., Grodzinsky, A. J., Zahn, M., & Pascual-Leone, A., [Transcranial direct current stimulation: a computer-based human model study](#), *NeuroImage*, **35** (3): 1113-1124 (2007)
- [13] Wen, H., [Noninvasive quantitative mapping of conductivity and dielectric distributions using RF wave propagation effects in high-field MRI](#), In *Proceedings of SPIE 5030, Medical Imaging: Physics of Medical Imaging, San Diego, California, USA*, 471-477 (2003)
- [14] Balidemaj, E., van den Berg, C. A., Trinks, J., van Lier, A. L., Nederveen, A. J., Stalpers, L. J. A., Crezee, H., & Remis, R. F., [CSI-EPT: A contrast source inversion approach for improved MRI-based electric properties tomography](#), *IEEE Trans Med Imaging*, **34** (9): 1788-1796 (2015)
- [15] Borsic, A., Perreard, I., Mahara, A., & Halter, R. J., [An inverse problems approach to MR-EPT image reconstruction](#), *IEEE Trans Med Imaging*, **35** (1): 244-256 (2016)
- [16] Wang, Y., Van de Moortele, P-F., & He, B., [Automated gradient-based electrical properties tomography in the human brain using 7 Tesla MRI](#), *Magnetic Resonance Imaging*, **63**: 258-266 (2019)
- [17] Liu, J., Zhang, X., Schmitter, S., Van de Moortele, P-F., & He, B., [Gradient-Based Electrical Properties Tomography \(gEPT\): A Robust Method for Mapping Electrical Properties of Biological Tissues In Vivo Using Magnetic Resonance Imaging](#), *Magnetic Resonance in Medicine*, **74** (3): 634-646 (2015)

-
- [18] Grattan-Guinness, I., & Yadav, B. S., [History of the Mathematical Sciences](#), Springer (2014).
- [19] Smith, S. W., [The Scientist and Engineer's Guide to Digital Signal Processing](#), California Technical Publishing (1997).
- [20] Bailey, D. H., & Swarztrauber, P. N., [A Fast Method for the Numerical Evaluation of Continuous Fourier and Laplace Transforms](#), *SIAM Journal on Scientific Computing*, **15** (5): 1105-1110 (1994).
- [21] Bracewell, N. B., [The Fourier Transform and Its Applications](#), *Electrical Engineering Series* (2000).
- [22] Ballard, D. H., & Brown, C. M., [Computer Vision](#), *Library of Congress Cataloging in Publication Data* (1982).
- [23] Nussbaumer, H. J., [Fast Fourier Transform and Convolution Algorithms](#), Springer (2012).
- [24] Wilmott, P., Howison, S., & Dewynne, J., [The Mathematics of Financial Derivatives, Student Introduction](#), Cambridge University Press (1995).
- [25] Olver, P., [Introduction to Partial Differential Equations](#), Springer (2013).
- [26] Fletcher, C., [Computational Techniques for Fluid Dynamics 1](#), Springer (1998).
- [27] Smith, N. B., & Webb, A., [Introduction to Medical Imaging, Physics, Engineering and Clinical Applications](#), Cambridge University Press (2010).
- [28] Stanisiz, G. J., Odrobina, E. E, Pun, J., Escavarage, M., Graham, S. J., Bronskill, M. J., & Henkelman, R. M., [T1, T2 Relaxation and Magnetization Transfer in Tissue at 3T](#), *Magnetic Resonance in Imaging*, **54** (3): 507-512 (2005)
- [29] Bottomley, P. A., Hardy, C. J, Argersinger, & Allen-Moore, G., [A review of ¹H nuclear magnetic resonance relaxation in pathology: Are T1 and T2 diagnostic?](#) , *Medical Physics*, **14** (1): 1-37 (1987)
- [30] van Lier, A. L. H. M. W., Brunner, D. O., Pruessmann, K. P., Klomp, D. W. J., Luijten, P. R., Lagendijk, J. J. W., & van den Berg, C. A. T., [B₁⁺ Phase Mapping at 7T and its Application for In Vivo Electrical](#)

- [Conductivity Mapping](#), *Magnetic Resonance in Medicine*, **67** (2): 552-561 (2012)
- [31] Canny, J., [A Computational Approach to Edge Detection](#), *IEEE Transactions on Pattern Analysis and Machine Intelligence*, **8** (6): 679-698 (1986)
- [32] Kelley, C., [Iterative Methods for Optimization](#), *the Society for Industrial and Applied Mathematics* (2011)
- [33] Dai, Y-H., [Nonlinear Conjugate Gradient Methods*](#), *Wiley Encyclopedia of Operations Research and Management Science*, (2011)
- [34] Piccolomini, E. L., & Zama, F., [The conjugate gradient regularization method in Computed Tomography problems](#), *Applied Mathematics and Computation*, **102** (1): 87-99 (1999)
- [35] Fletcher, R., & Reeves, C. M., [Function minimization by conjugate gradients](#), *Comput. J.*, **7** (2): 149-154 (1964)
- [36] Bovik, A., [Handbook of Image and Video Processing](#), *Southern Methodist University*, (2000)
- [37] Hewitt, E., & Hewitt, R. E., [The Gibbs-Wilbraham Phenomenon: An Episode in Fourier Analysis](#), *Archive for History of Exact Sciences*, **21** (2): 129-160 (1979)
- [38] Barzilai, J., & Borwein, J. M., [Two-Point Step Size Gradient Methods](#), *IMA Journal of Numerical Analysis*, **8** (1): 141-148 (1988)
- [39] Ito, K., & Xiong, K., [Gaussian filters for nonlinear filtering problems](#), *IEEE Transactions on Automatic Control*, **45** (5): 910-927 (2000)
- [40] Muir, E. R., Cardenas, D., Huang, S., Roby, J., Li, G., & Duong, T. Q., [MRI under hyperbaric air and oxygen: effects on local magnetic field and relaxation times](#), *Magnetic Resonance in Medicine*, **72** (4): 1176-1781 (2013)
- [41] Huijnen, L., [MSc Thesis: Evaluating phase-only EPT for the clinical assessment of breast lesions](#), *Leiden University*, (2019)
- [42] Charbonnier, P., Blanc-Feraud, L., Aubert, G., & Barlaud, M., [Two deterministic half-quadratic regularization algorithms for computed imaging](#), *In Proceedings of IEEE International Conference on Image Processing*, **2**: 168-171 (1994)

Attachments

Appendix A

Gradients of Inner Products

Let

$$f(\mathbf{x}) = \mathbf{a}^T \mathbf{x},$$

where \mathbf{a} is a constant vector. The function, then, can be defined

$$f(\mathbf{x}) = \sum_{i=1}^n a_i x_i,$$

where a_i and x_i are components of the vectors \mathbf{a} and \mathbf{x} , respectively. If we take derivative of the function with respect to \mathbf{x} , we have

$$\frac{\partial f}{\partial x_j} = \sum_{i=1}^n c_i \delta_{ij} = c_j,$$

where δ_{ij} is Kronecker delta

$$\delta_{ij} = \begin{cases} 0 & \text{if } i \neq j; \\ 1 & \text{if } i = j. \end{cases}$$

Therefore, the gradient of the function

$$\nabla f(\mathbf{x}) = \mathbf{a}.$$

Now, let

$$g(\mathbf{x}) = \mathbf{x}^T A \mathbf{x} = \sum_{i=1}^n \sum_{j=1}^n b_{ij} x_i x_j.$$

Then

$$\begin{aligned} \frac{\partial g}{\partial x_k} &= \sum_{i=1}^n \sum_{j=1}^n b_{ij} \frac{\partial x_i x_j}{\partial x_k} \\ &= \sum_{i=1}^n \sum_{j=1}^n b_{ij} (\delta_{ik} x_j + x_i \delta_{jk}) \\ &= \sum_{j=1}^n b_{kj} x_j + \sum_{i=1}^n b_{ik} x_i \\ &= A \mathbf{x} + A^T \mathbf{x}. \end{aligned}$$

Hence we conclude that

$$\nabla g(\mathbf{x}) = (A + A^T) \mathbf{x}.$$

Gradient of 2-norm of Residual Vector

Definition of a norm is

$$\|\mathbf{x}\|_2 = \sqrt{\mathbf{x}^T \mathbf{x}},$$

so we can expand squared 2-norm of residual vector

$$\begin{aligned} \|\mathbf{a} - B\mathbf{x}\|^2 &= (\mathbf{a} - B\mathbf{x})^T (\mathbf{a} - B\mathbf{x}) \\ &= \|\mathbf{a}\|^2 - (B\mathbf{x})^T \mathbf{a} - \mathbf{a}^T (B\mathbf{x}) + \mathbf{x}^T B^T B \mathbf{x} \\ &= \|\mathbf{a}\|^2 - 2\mathbf{a}^T (B\mathbf{x}) + \mathbf{x}^T B^T B \mathbf{x} \\ &= \|\mathbf{a}\|^2 - 2(B^T \mathbf{a})^T \mathbf{x} + \mathbf{x}^T B^T B \mathbf{x}, \end{aligned}$$

where we used property of a transpose $(\mathbf{ab})^T = \mathbf{b}^T \mathbf{a}^T$ and commutativity assumption.

Using the gradients of inner products specified in the previous page, mainly

$$\nabla(\mathbf{c}^T \mathbf{x}) = \mathbf{c},$$

where $\mathbf{c} = B^T \mathbf{a}$ and

$$\nabla(\mathbf{x}^T A \mathbf{x}) = (A + A^T) \mathbf{x},$$

where $A = B^T B$ giving us

$$\nabla \|\mathbf{a} - B\mathbf{x}\|^2 = -2B^T \mathbf{a} + (B^T B + (B^T B)^T) \mathbf{x}.$$

Since

$$(B^T B)^T = B^T (B^T)^T = B^T B,$$

the gradient of the squared norm of the vector residual reduces to

$$\nabla \|\mathbf{a} - B\mathbf{x}\|^2 = -2B^T \mathbf{a} + 2B^T B \mathbf{x} = 2B^T (B\mathbf{x} - \mathbf{a}).$$

This result applies to two-dimensional maps as well as for the maps of higher dimensions as long as we remember to replace transpose with adjoints of the matrices.

Appendix B

Proof of $L(\mathbf{a} + \mathbf{b}) = L\mathbf{a} + L\mathbf{b}$

$$\begin{aligned}
 L(\mathbf{a} + \mathbf{b}) &:= L * (\mathbf{a} + \mathbf{b}) \\
 &= \mathcal{F}^{-1}\{\mathcal{F}\{L\} \cdot \mathcal{F}\{\mathbf{a} + \mathbf{b}\}\} \\
 &= \mathcal{F}^{-1}\{\mathcal{F}\{L\} \cdot (\mathcal{F}\{\mathbf{a}\} + \mathcal{F}\{\mathbf{b}\})\} \\
 &= \mathcal{F}^{-1}\{\mathcal{F}\{L\} \cdot \mathcal{F}\{\mathbf{a}\} + \mathcal{F}\{L\} \cdot \mathcal{F}\{\mathbf{b}\}\} \\
 &= \mathcal{F}^{-1}\{\mathcal{F}\{L\} \cdot \mathcal{F}\{\mathbf{a}\}\} + \mathcal{F}^{-1}\{\mathcal{F}\{L\} \cdot \mathcal{F}\{\mathbf{b}\}\} \\
 &= L\mathbf{a} + L\mathbf{b} \tag{5.1}
 \end{aligned}$$

where we used simplified notation $L\mathbf{a} := L * \mathbf{a}$ which was mentioned in equation (3.20).